ATLAS CONF Note

ATLAS-CONF-2021-007

22nd March 2021

Search for R-parity violating supersymmetry in a final state containing leptons and many jets with the ATLAS experiment using $\sqrt{s} = 13$ TeV proton–proton collision data

The ATLAS Collaboration

A search for R-parity violating supersymmetry in final states characterised by high jet multiplicity, at least one isolated light lepton and either zero or at least three b-tagged jets is presented. The search uses $139\,\text{fb}^{-1}$ of $\sqrt{s} = 13$ TeV proton–proton collision data collected by the ATLAS experiment during Run 2 of the Large Hadron Collider. The results are interpreted in the context of R-parity-violating supersymmetry models that feature gluino production, top-squark production, or electroweakino production. The dominant sources of background are estimated using a data-driven model, based on observables at medium jet multiplicity, to predict the b-tagged jet multiplicity distribution at the higher jet multiplicities used in the search. Machine learning techniques are used to reach sensitivity to electroweakino production, extending the data-driven background estimation to the shape of the machine learning discriminant. No significant excess over the Standard Model expectation is observed and exclusion limits at the 95% confidence-level are extracted, reaching as high as 2.4 TeV in gluino mass, 1.35 TeV in top-squark mass, and 320 (365) GeV in higgsino (wino) mass.

1 Introduction

Supersymmetry (SUSY) [1–6] is a theoretical extension of the Standard Model (SM) which fundamentally relates fermions and bosons. It is an alluring theoretical possibility given its potential to solve the hierarchy problem [7–10]. An ad-hoc conserved quantity, R-parity [11], is often introduced in SUSY models to avoid rapid proton decay, rendering the lightest supersymmetric particle (LSP) stable and therefore a potential dark matter candidate [12, 13]. There is no fundamental theoretical reason for strictly imposing R-parity conservation, and R-parity violating (RPV) SUSY models are well motivated, with fewer experimental constraints than many R-parity conserving (RPC) models [14, 15], and allow for more natural supersymmetric mass spectra.

This article presents a search for pair production of supersymmetric particles with subsequent RPV decays in final states with at least one isolated lepton (electron or muon), at least eight to fifteen jets (depending on the jet transverse momentum threshold), and either zero or many jets containing b-flavoured hadrons (b-jets), and with no requirement on the missing transverse momentum. Such a final state is commonly predicted in RPV models with either baryon-number-violating [16, 17] or lepton-number-violating couplings [18]. Events are split in two categories according to the lepton content. The first category contains events with two leptons with same electric charge ($2\ell^{\mathrm{sc}}$), while the second category contains all other events and is dominated by single-lepton events (1ℓ). Electrons and muons from τ-lepton decays are also considered. A multi-bin fit in each lepton category to the two-dimensional space of jet-multiplicity and b-jet multiplicity is used to constrain parameters of benchmark RPV simplified signal models [19–21]. A third variable, based on a machine-learning discriminant, is introduced to improve the sensitivity of the search when testing for the electroweak production of supersymmetric particles. This search has potential sensitivity to a large number of beyond the Standard Model (BSM) physics models, and model independent limits on the possible contribution of BSM physics to several single-bin signal regions are shown.

The dominant Standard Model background in the 1ℓ category arises from top-quark pair production and W/Z + jets production, with at least one lepton produced in the vector boson decay. In the $2\ell^{\mathrm{sc}}$ category the associated production of a top-quark pair and a W boson ($t\bar{t}W$), as well as top-quark pair production with a misidentified lepton constitute the main backgrounds. The theoretical modelling of these backgrounds at high jet multiplicity suffers from large uncertainties, so they are estimated from the data by extrapolating the b-jet multiplicity distribution extracted at moderate jet multiplicities to the high jet multiplicities of the search region.

This analysis is an update to a previous ATLAS search for new phenomena in a lepton plus high jet multiplicity final state presented in Ref. [22], which was performed with 36 fb^{-1} of $\sqrt{s} = 13$ TeV proton–proton collision data. It improves over the previous result owing to the larger luminosity, the dedicated categorisation and analysis of events with two leptons with the same electric charge, as well as the introduction of multivariate discriminants. This search represents the first LHC result to obtain sensitivity to electroweak production of SUSY particles promptly decaying to quarks, as predicted in baryon-number-violating RPV models. Previous searches targeting similar RPV SUSY models have been carried out by the ATLAS and CMS collaborations [23–32]. The result is also sensitive to the SM four-top-quark production and a validation of the background estimation methods is performed by fitting the normalisation of the four-top process relative to the Standard Model value. Previous searches for four-top-quark production were carried out by the ATLAS [33] and CMS collaborations [34].

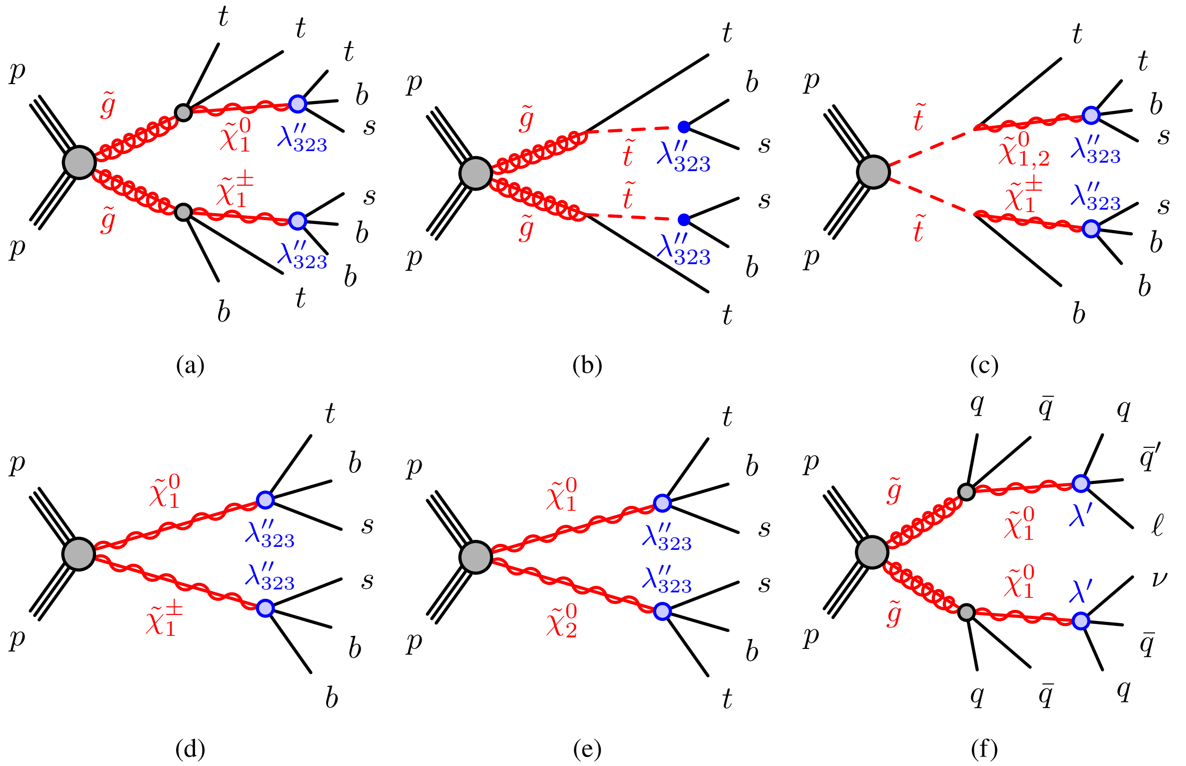

Figure 1: Examples of signal diagrams for the simplified RPV models considered in the paper. Cases where both the gluino (or the stop) decays in the same way are also considered. The $\tilde{\chi}_1^\pm \tilde{\chi}_2^0$ pair production is also considered for the higgsino LSP type.

2 Signal models

Simulated signal events from five SUSY benchmark simplified models (Figure 1) are used to guide the analysis selections and to estimate the expected signal yields for different signal-mass hypotheses used to interpret the analysis results. In all models considered, the RPV couplings and the SUSY particle masses are chosen to ensure prompt decays of the SUSY particles. Scenarios that could result in long-lived SUSY particles are not covered in this paper, but are widely studied in ATLAS [35, 36]. Four of the simplified models are inspired by a common natural RPV SUSY model assuming the minimal flavour violation hypothesis [16, 17]. The sparticle content of the models is the partner of the SM gluon (gluino), the partner of the right-handed top-quark (stop), and electroweakinos. The electroweakinos ($\tilde{\chi}_1^0$, $\tilde{\chi}_2^0$ and $\tilde{\chi}_1^\pm$) are massive fermions resulting from the mixing between the partners of SM electroweak and Higgs bosons[1]. Three different possibilities for the electroweakino composition are tested: pure bino, pure wino or pure higgsino. In all cases the lightest neutralino ($\tilde{\chi}_1^0$) is the LSP. When considering a wino (higgsino) LSP, the corresponding chargino $\tilde{\chi}_1^\pm$ (and second neutralino $\tilde{\chi}_2^0$) is assumed to be mass degenerate with the LSP and considered both in production and decay processes. The gluino and stop branching ratios, as well as the electroweakino production cross-section, are determined by the nature of the electroweakino. Table 1 summarises the gluino and stop branching ratios, and shows example cross-sections for direct electroweakino productions [37–41], for each electroweakino type. The electroweakinos decay in all cases

---

[1] In SUSY, the Higgs sector is enriched by the presence of an additional complex doublet.

LSP	Branching ratios for sparticle:					Cross-section [fb]		
type	stop		gluino			for direct production		
	$t\tilde{\chi}^0_{1,2}$	$b\tilde{\chi}^\pm_1$	$tt\tilde{\chi}^0_{1,2}$	$bb\tilde{\chi}^0_{1,2}$	$tb\tilde{\chi}^\pm_1$	$\tilde{\chi}^\pm_1\tilde{\chi}^0_1$	$\tilde{\chi}^\pm_1\tilde{\chi}^0_2$	$\tilde{\chi}^0_2\tilde{\chi}^0_1$
Bino	100%	0%	100%	0%	0%	0	0	0
Wino	33%	66%	16%	16%	66%	387	0	0
Higgsino	50%	50%	50%	0%	50%	91	91	52

Table 1: Stop and gluino branching rations, as well as cross-sections for direct electroweakino production, as a function of the LSP type. There is no $\tilde{\chi}^0_2$ component for the pure wino and pure bino LSP types. When relevant, decays to $\tilde{\chi}^0_1$ and $\tilde{\chi}^0_2$ are merged as they are assumed to be mass degenerate and both decay in the same way. The production cross-sections are given for an electroweakino mass of m($\tilde{\chi}^0_1$,$\tilde{\chi}^\pm_1$,$\tilde{\chi}^0_2$) = 300 GeV.

through a non-zero RPV coupling large enough to ensure to ensure prompt decays for the particle masses considered, and small enough to avoid more complex decay patterns involving mixtures of both RPC and RPV decays that are not considered here. Within this the analysis results are independent of the value of the coupling. The coupling λ''_{323} is chosen as it is predicted to be dominant under the minimal flavour violation hypothesis.[2] With the chosen model parameters, the electroweakinos decay as $\tilde{\chi}^0_{1/2} \rightarrow tbs$ and $\tilde{\chi}^\pm_1 \rightarrow bbs$, with a branching ratio of 100%. Signal events in these models contain four, six, or eight b-jets in the final state, depending on the production mode.

In the first model, gluino production is considered, with decays to heavy flavour quarks and the electroweakino, which in turn decays via the RPV coupling. The stop mass is assumed to be above the gluino mass, and not considered in the model. A signal diagram for this model is shown in Figure 1(a). The second model considers gluino pair production, with each gluino decaying to a top quark and a stop, as shown in Figure 1(b). In this model the RPV coupling is assumed to be large, so that the stop decays via RPV to an s-quark and a b-quark. The absence of RPC decays of the stop render the electroweakino mass irrelevant in this model. The third scenario considered involves stop pair production with the stop decaying to an electroweakino and a top or bottom quark, and the gluino set to a very high mass and not considered in the model. An example signal diagram is shown in Figure 1(c). In the fourth model, only electroweakino production is considered, with the stop and gluino set to a very high mass and not considered in the model. The $\tilde{\chi}^\pm_1\tilde{\chi}^0_1$ production is considered (Figure 1(d)), and in the case of higgsino LSP also the production of $\tilde{\chi}^\pm_1\tilde{\chi}^0_2$ and $\tilde{\chi}^0_1\tilde{\chi}^0_2$ (Figure 1(e)). The $\tilde{\chi}^\pm_1\tilde{\chi}^0_{1,2}$ production contributes only to the 1ℓ category, while the $\tilde{\chi}^0_1\tilde{\chi}^0_2$ production contributes to both 1ℓ and $2\ell^{\text{sc}}$ categories. The $\tilde{\chi}^\pm_1\tilde{\chi}^\pm_1$ production is not considered as it decays to a final state with no leptons.

The fifth and last simplified RPV model considers gluino pair production, where each gluino decays to two first or second generation quarks ($q \equiv (u, d, s, c)$) and the $\tilde{\chi}^0_1$ is the LSP. The $\tilde{\chi}^0_1$ decays to two additional first or second generation quarks and a charged lepton or a neutrino ($\tilde{\chi}^0_1 \rightarrow q\bar{q}'\ell$ or $\tilde{\chi}^0_1 \rightarrow q\bar{q}\nu$, labelled as $\tilde{\chi}^0_1 \rightarrow q\bar{q}\ell/\nu$). The decay proceeds via a λ' RPV coupling, where each RPV decay can produce any of the four first and second generation leptons ($e^\pm$, $\mu^\pm$, ν_e, ν_μ) with equal probability. An example signal diagram is shown in Figure 1(f). Signal decays from this model yield a final state with high jet multiplicity and zero b-jets.

---

[2] The results apply equally to the coupling λ''_{313} since it leads to the same experimental final state.

3 ATLAS detector

The ATLAS experiment [42] at the LHC is a multipurpose particle detector with a forward–backward symmetric cylindrical geometry and nearly 4π coverage in solid angle.[3] It consists of an inner tracking detector (ID) surrounded by a thin superconducting solenoid providing a 2 T axial magnetic field, electromagnetic (EM) and hadron calorimeters, and a muon spectrometer (MS). The inner tracking detector covers the pseudorapidity range $|\eta| < 2.5$. It consists of silicon pixel, silicon microstrip and transition radiation tracking detectors; the innermost layer is 33 mm from the beamline [43, 44]. Lead/liquid-argon (LAr) sampling calorimeters provide electromagnetic energy measurements with high granularity. A steel/scintillator-tile hadron calorimeter covers the central pseudorapidity range ($|\eta| < 1.7$). The endcap and forward regions are instrumented with LAr calorimeters for both the EM and hadronic energy measurements up to $|\eta| = 4.9$. The muon spectrometer surrounds the calorimeters and is based on three large superconducting air-core toroidal magnets with eight coils each. The field integral of the toroids ranges between 2.0 and 6.0 T·m across most of the detector. The muon spectrometer includes a system of precision tracking chambers and fast detectors for triggering. A two-level trigger system is used to select events [45]. The first-level trigger is implemented in hardware and uses a subset of the detector information to keep the accepted rate below approximately 100 kHz. This is followed by a software-based trigger that reduces the accepted event rate to approximately 1 kHz on average depending on the data-taking conditions.

4 Monte Carlo event simulation

Signal and background events produced in proton–proton collisions were simulated with various Monte Carlo (MC) generators. The simulated events are used in the optimisation of event selection criteria, in the neural network training, to estimate systematic uncertainties, validate the background estimation procedure employed for the dominant background sources, and to predict yields for the subdominant background contributions and for possible signals. The signal and background events were passed through the GEANT4 [46] simulation of the ATLAS detector [47] and reconstructed using the same algorithms as are used for the data.

The generation of the simulated event samples includes the effect of multiple proton–proton interactions per bunch crossing, as well as the impact on the detector response due to interactions from bunch crossings before or after the one containing the hard interaction. The effect of multiple interactions in the same and neighbouring bunch crossings (pile-up) is modelled by overlaying simulated inelastic proton–proton events generated with PYTHIA 8.186 [48] using the `NNPDF2.3lo` set of parton distribution functions (PDF) [49] and the A3 tuned parameters of the MC programs [50] over the original hard-scattering event. The MC events are weighted to reproduce the distribution of the average number of interactions per bunch crossing ($\langle\mu\rangle$) observed in the data. The EVTGEN [51] program was used to simulate properties of the b- and c-flavoured hadron decays.

---

[3] ATLAS uses a right-handed coordinate system with its origin at the nominal interaction point (IP) in the centre of the detector and the z-axis along the beam pipe. The x-axis points from the IP to the centre of the LHC ring, and the y-axis points upwards. Cylindrical coordinates (r, ϕ) are used in the transverse plane, ϕ being the azimuthal angle around the z-axis. The pseudorapidity is defined in terms of the polar angle θ as $\eta \equiv -\ln\tan(\theta/2)$, and is equal to the rapidity $y \equiv 0.5\ln((E + p_z)/(E - p_z))$ in the relativistic limit. Angular distance is measured in units of $\Delta R \equiv \sqrt{(\Delta y)^2 + (\Delta\phi)^2}$. The magnitude of the momentum in the plane transverse to the beam axis is denoted by p_{T}.

The signal event samples were generated using MadGraph5_aMC@NLO [52] generator interfaced to Pythia 8 for the modelling of the parton showering, hadronisation, and underlying event. The matrix element (ME) calculation was performed at tree-level and includes the emission of up to two additional partons. The signal samples were processed through a fast simulation of the ATLAS detector [53, 54]. Gluino and stop signal cross-sections are calculated to approximate next-to-next-to-leading order in the strong coupling constant, adding the resummation of soft gluon emission at next-to-next-to-leading-logarithmic accuracy (approximate NNLO+NNLL) [55–65]. The cross-sections for electroweakino production are calculated to next-to-leading order in the strong coupling constant, adding the resummation of soft gluon emission at next-to-leading-logarithmic accuracy (NLO+NLL) [37–41].

Physics process	Event generator	Parton-shower modelling	Cross-section normalisation	PDF set	Tune
$W(\to \ell\nu)$ + jets	Sherpa 2.2.1 [66]	Sherpa 2.2.1	NNLO [67]	`NNPDF3.0nnlo` [68]	Sherpa
$W(\to \ell\nu)$ + jets (*)	MG5_aMC 2.2.2 [52]	Pythia 8.186 [69]	NNLO	`NNPDF3.0nlo` [68]	A14 [70]
$Z/\gamma^*(\to \ell\ell)$ + jets	Sherpa 2.2.1	Sherpa 2.2.1	NNLO [67]	`NNPDF3.0nnlo`	Sherpa
$t\bar{t}$ + jets	PowhegBox v2 [71–74]	Pythia 8.230 [48]	NNLO+NNLL [75–81]	`NNPDF3.0nlo`	A14
$t\bar{t}$ + jets (*)	PowhegBox v2	Herwig7.04 [82, 83]	NNLO+NNLL	`MMHT2014lo` [84]	H7UE [83]
$t\bar{t}$ + jets (*)	MG5_aMC 2.6.0	Pythia 8.230	NNLO+NNLL	`NNPDF3.0nlo`	A14
Single-top	PowhegBox v2 [85–87]	Pythia 8.230	NNLO+NNLL [88–90]	`NNPDF3.0nlo`	A14
$t\bar{t} + W/Z$	Sherpa 2.2.1	Sherpa 2.2.1	NLO [91]	`NNPDF3.0nnlo`	Sherpa
$t\bar{t} + t\bar{t}/t/WW/WZ$	MG5_aMC 2.3.3 [52]	Pythia 8.230	NLO [91] ($t\bar{t}t$ LO)	`NNPDF2.3lo` [49]	A14
$t\bar{t}t\bar{t}$ (*)	MG5_aMC 2.3.3	Herwig7.04	NLO [52]	`MMHT2014lo`	H7UE
$t\bar{t}H$	PowhegBox v2	Pythia 8.230	NLO	`NNPDF3.0nlo`	A14
tWZ, tZ	MG5_aMC 2.3.3	Pythia 8.212, 8.210	NLO	`NNPDF3.0nlo`	A14
VV and VVV	Sherpa 2.2.1, 2.2.2, 2.2.4	Sherpa	NLO	`NNPDF3.0nnlo`	Sherpa

Table 2: Simulated background event samples: the corresponding event generator, parton-shower modelling, cross-section normalisation, PDF set and underlying-event tune are shown. The samples marked with (*) are alternative samples used to validate the background estimation method or to assess systematic uncertainties on the modelling. The abbreviation MG5_aMC is used to label the MadGraph5_aMC@NLO generator. Samples produced with Sherpa use the default set of tuned parameters of the generator.

The production of $t\bar{t}$, $t\bar{t}H$, and single-top events were modelled at NLO using the PowhegBox [71–74, 92] generator. Additional $t\bar{t}$ samples were generated with MadGraph5_aMC@NLO interfaced with Pythia 8, and PowhegBox interfaced with Herwig7 [82, 83] for modelling comparisons and evaluation of systematic uncertainties.

The production of $t\bar{t}V$ ($V = W$, Z) events was modelled using the Sherpa generator. The ME was calculated for up to one additional parton at NLO and up to two partons at LO using COMIX [93] and OpenLoops library [94, 95], and merged with the Sherpa parton shower using the MEPS@NLO prescription [96–100]. Alternative $t\bar{t}V$ samples produced with MadGraph5_aMC@NLO generator at NLO were used to evaluate systematic uncertainties associated with the modelling of additional QCD radiation.

The production of $t\bar{t}t\bar{t}$, $t\bar{t}t$, tWZ, tZ, $t\bar{t}WW$, and $t\bar{t}WZ$ events was modelled using the MadGraph5_aMC@NLO generator at NLO, and interfaced with Pythia 8. An alternative $t\bar{t}t\bar{t}$ sample showered with Herwig7, was used to evaluate systematic uncertainties related to the choice of shower.

The production of an electroweak gauge boson or virtual photon in association with jets (V+jets) was simulated with the Sherpa generator using NLO matrix elements for up to two partons, and LO matrix elements for up to four partons. Alternative V+jets samples used to validate the analysis methods were simulated using LO-accurate ME with up to four final-state partons with MadGraph5_aMC@NLO.

Event samples of diboson (VV) and triboson (VVV) final states were simulated with the Sherpa generator, including off-shell effects and Higgs boson contributions, where appropriate. The VV processes were simulated using matrix elements at NLO accuracy in QCD for up to one additional parton and at LO accuracy for up to three additional parton emissions. The production of triboson (VVV) events was simulated with the Sherpa generator using factorised gauge-boson decays.

A summary of the background samples used together with the event generator configurations can be found in Table 2.

5 Event reconstruction and object identification

Proton–proton collision data recorded by the ATLAS detector between 2015 and 2018 is used to perform the analysis. In this period, the LHC delivered colliding beams with a peak instantaneous luminosity up to $L = 2.1 \times 10^{34}\,\text{cm}^{-2}\text{s}^{-1}$, achieved in 2018, and an average number of pp interactions per bunch crossing of 33.7. After applying beam, detector, and data-quality criteria the total integrated luminosity of the data set corresponds to 139 fb^{-1} [101]. The uncertainty in the combined 2015–2018 integrated luminosity is 1.7% [102], obtained using the LUCID-2 detector [103] for the primary luminosity measurements.

Proton–proton interaction vertices are reconstructed from charged-particle tracks with $p_{\text{T}} > 500$ MeV [104, 105] in the ID. The presence of at least one such vertex with a minimum of two associated tracks is required, and the vertex with the largest sum of p_{T}^2 of associated tracks is chosen as the primary vertex.

Jet candidates are reconstructed up to $|\eta| = 4.9$ using the anti-k_t algorithm [106, 107] with radius parameter $R = 0.4$. It uses particle-flow objects as inputs, combining tracking and calorimetric information as detailed in Ref. [108]. The jets are calibrated using the methodology described in Ref. [109]. Any event that contains jets induced by calorimeter noise or non-collision background, according to criteria similar to those described in Ref. [110], is removed. Jets up to $p_{\text{T}} = 60$ GeV containing a large energy contribution from pile-up interactions are suppressed with the jet-vertex tagging (JVT) algorithm that uses tracking and primary vertex information to determine if a given jet originates from the primary vertex [111]. Jets with $p_{\text{T}} > 20$ GeV and $|\eta| < 2.5$ are defined as signal jets.

Signal jets containing b-flavoured hadrons are identified with the DL1r b-tagging algorithm [112, 113] with an average identification efficiency of 70% in simulated $t\bar{t}$ events. The rejection factor is measured to be approximately 300 for jets initiated by light quarks and gluons and approximately 9 for jets initiated by charm quarks [114].

Electron candidates are reconstructed as tracks in the ID matched to energy clusters in the EM calorimeter, within $|\eta| < 2.47$ [115]. In the analysis only candidate electrons with $p_{\text{T}} > 10$ GeV and not in the transition region between the barrel and endcap calorimeters ($1.37 < |\eta| < 1.52$) are considered. The electron identification is based on a multivariate likelihood-based discriminant that uses the shower shapes in the EM calorimeter and the associated track properties measured in the ID. The electron candidates must satisfy the 'Medium' identification criteria described in Ref. [115], while the signal electrons must satisfy the 'Tight' identification for better rejection of non-prompt or misidentified electrons. The electron identification efficiency varies with increasing p_{T} in $Z \to ee$ events, from 65% at $p_{\text{T}} = 10$ GeV to 88% at 100 GeV for the Tight operating point, and from 75% at 20 GeV to 94% at 100 GeV for the Medium operating point.

For candidate and signal electrons, the longitudinal impact parameter of the electron track, z_0, is required to satisfy $|z_0 \sin\theta| < 0.5$ mm, where θ is the polar angle of the track. For signal electrons, the transverse impact parameter divided by its uncertainty, $|d_0|/\sigma(d_0)$, is required to be at most five.

For all signal electrons there must be no association with a vertex from a reconstructed photon conversion [115] in the detector material. To further reduce the photon conversion background, additional requirements are applied to the signal electrons [33]: i) the candidate must not have a reconstructed displaced vertex with a conversion radius $r > 20$ mm whose reconstruction uses the track associated with the electron, ii) the invariant mass of the system formed by the track associated with the electron and the closest track (in ΔR) at the primary or a conversion vertex is required to be larger than 100 MeV. This photon conversion veto has an average efficiency of 99% for prompt electrons while providing a rejection factor of 4 for electrons from photon conversion.

In the $2\ell^{\text{sc}}$ category, signal electrons with wrongly reconstructed charge (charge-flip) are suppressed using a boosted decision tree discriminant exploiting additional tracks in the vicinity of the electron and track-to-cluster matching variables [115]. A rejection factor of around 9 for electrons with a wrong charge assignment is achieved, while selecting properly measured electrons with an efficiency of 98%, in simulated $Z \to ee$ events selected with the Tight identification and isolation operating points [115].

Muon candidates are reconstructed in the region $|\eta| < 2.5$ from MS tracks matching ID tracks. Only muons with $p_{\text{T}} > 10$ GeV satisfying the 'Medium' quality requirements defined in Ref. [116] are considered. The muon reconstruction efficiency is approximately 98% in simulated $Z \to \mu\mu$ events. The same longitudinal impact parameter selection as for candidate and signal electrons is considered, while $|d_0|/\sigma(d_0)$ is required to be at most three.

For signal electrons and muons the identification criteria are complemented by an isolation requirement, which is based on the energy in a cone around the lepton candidate calculated using either reconstructed tracks or energy clusters. Non-prompt electrons and muons from the decays of b- and c-flavoured hadrons are further rejected using a boosted decision tree discriminant based on isolation and secondary vertex information, referred to as the non-prompt-lepton veto [117]. The efficiency of the combined isolation and non-prompt-lepton veto is on average above 80% for prompt leptons with $p_{\text{T}} > 30$ GeV in simulated di-boson events.

A sequential overlap removal procedure is carried out to resolve ambiguities between candidate jets and candidate leptons before the signal selection as follows. First, candidate electrons sharing their track with a muon candidate are removed. Furthermore, any non-b-jet candidate lying within an angular distance $\Delta R = 0.2$ of a candidate electron is discarded; non-b-jets within $\Delta R = 0.4$ of candidate muons are removed if the number of tracks associated with the jet is less than three. Finally, any lepton candidate remaining within a distance $\Delta R > \min\{0.4, 0.04 + 10\,\text{GeV}/p_{\text{T}}(\ell)\}$ of any surviving jet candidate is discarded since they likely arise from b- and c-flavoured hadrons decays.

Similar to the electron candidates, the photon candidates are reconstructed from calorimeter clusters and identified using the 'Tight' criteria [115]. They are required to be in the region $|\eta| < 2.37$ and have $p_{\text{T}} > 145$ GeV. Signal photons are required to satisfy the 'Tight' calorimeter-based isolation requirements [115], and are used to validate the background technique detailed in section 7.1.

The missing transverse momentum, with magnitude $E_{\text{T}}^{\text{miss}}$, is defined as the negative vector sum of the transverse momenta of all identified objects (muon, electron and jet candidates) and an additional soft term [118, 119]. The soft term is added to recover the contributions from other low-p_{T} objects, and is constructed from all tracks that are matched to the primary vertex and are not associated with any other object. A dedicated overlap removal procedure, based on removing duplicated energy contributions, is applied. The $E_{\mathrm{T}}^{\mathrm{miss}}$ variable is used to define control regions enriched in certain types of background, as discussed in section 7.4, and as input for the multivariate discriminant.

6 Event selection and analysis strategy

Two complementary analysis strategies are defined, namely the *'jet counting analysis'* and the electroweak analysis, labelled *'EWK analysis'*. While the first approach is designed to be very generic and offers a large variety of signal interpretations for strong production models, the second approach is specifically tailored to reach sensitivity in the electroweakino production. In both analyses, events are split in two categories according to the lepton content, and further categorised in regions based on the jet multiplicity and b-jet multiplicity. The EWK analysis is an extension of the jet counting analysis, where a third variable, a neural network (NN) discriminant, is introduced in some of the jet and b-jet multiplicity regions in order to improve the signal separation. Additional kinematic selections are also applied at the preselection level, tailored to the electroweakino signals.

Events are selected for read-out using single-lepton triggers that require the electron or muon to satisfy identification criteria similar to those used in the offline reconstruction and isolation criteria [120, 121]. For the analysis selection, at least four jets and at least one signal electron or muon, matched to the trigger lepton, are required in the event. All signal leptons are required to have $p_{\mathrm{T}} > 15\,\mathrm{GeV}$, while the highest-$p_{\mathrm{T}}$ lepton in the event has to pass the signal requirements and satisfy $p_{\mathrm{T}} > 27\,\mathrm{GeV}$, in order to be above the trigger threshold. Two disjoint event categories are defined according to the lepton content: an inclusive selection with at least one lepton (1ℓ), and a same-charge dilepton selection ($2\ell^{\mathrm{sc}}$). Events are placed in the $2\ell^{\mathrm{sc}}$ category if they contain exactly two signal leptons with same electric charge, and no additional candidate leptons. In order to reduce backgrounds containing a Z boson decaying to electrons, where an electron has its charge misidentified, events with two electrons have to satisfy the $|m_{ee} - m_Z| > 10\,\mathrm{GeV}$ requirement. Events with at least three signal leptons, with one same-flavour pair satisfying $|m_{ll} - m_Z| < 10\,\mathrm{GeV}$ and exactly zero b-jets, are also included in the $2\ell^{\mathrm{sc}}$ category and used for the background estimation. All events passing further selections which do not enter in the $2\ell^{\mathrm{sc}}$ category, are assigned to the 1ℓ category, including events containing more than one candidate lepton. The regions with fewer than or equal to 7 jets, and 0 b-jets in the 1ℓ category are further divided into three subregions. The first subregion is defined by selecting events with two same-flavour candidate leptons fulfilling an invariant-mass requirement, $|m_{ll} - m_Z| < 10\,\mathrm{GeV}$. The remaining events are divided into two subregions according to the electric charge of the highest-p_{T} lepton.

The jet counting analysis is carried out with five jet p_{T} thresholds to provide sensitivity to a broad range of possible signals. These thresholds are applied to all jets in the event and are p_{T} = 20, 40, 60, 80, and 100 GeV. The jet multiplicity is binned from a minimum of four jets to a maximum number that depends on the p_{T} threshold and the lepton category. This bin corresponds in the 1ℓ category to 15 or more jets for the 20 GeV requirement, and 12, 11, 10, 8 jets for the rest of thresholds in increasing order. In the $2\ell^{\mathrm{sc}}$ category it corresponds to 10, 8, 7, 7, 6 jets respectively. The highest jet multiplicity bin is inclusive of larger jet multiplicities. There are five bins in the b-jet multiplicity (exclusive bins from zero to three with an additional inclusive four-or-more bin). The number of bins used in the search ranges from 110 when considering the 20 GeV jet threshold, including the different subregions with 0 b-jets, to 54 bins when considering the 100 GeV jet threshold. In this article, the notation $N_{j,b}^{\mathrm{process}}$ is used to denote the number of events predicted by the background fit model, with j jets and b b-jets for a given process, e.g. $N_{j,b}^{t\bar{t}\,\mathrm{+jets}}$

for $t\bar{t}$+jets events. N_j^{process}, referred to as jet slice, is the number of events with j jets for the considered physics process, and it is inclusive in the number of b-jets.

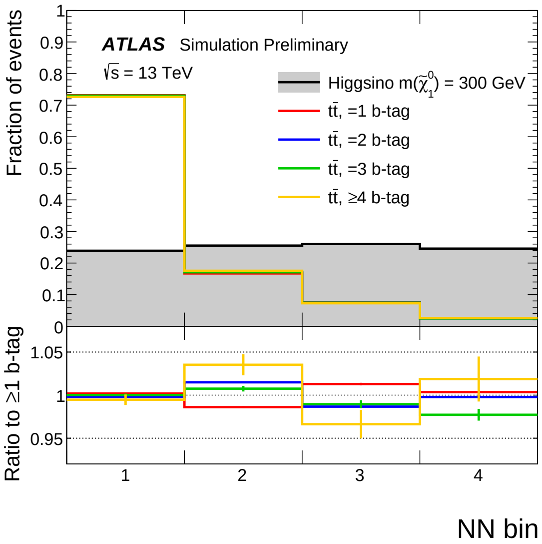

Figure 2: Output distribution of the NN discriminant in the 6-jet slice, evaluated over a signal sample and $t\bar{t}$ background split in the different b-jet regions. The bottom panel shows the ratio of the NN output distribution for $t\bar{t}$ background in each b-jet region with respect to the distribution in an inclusive region with at least one b-jet. The NN output distribution is invariant with respect to the number of b-jets in the selection, with differences per bin below 4%.

In order to improve the sensitivity of the search to the model with electroweakino production, the EWK analysis is introduced, which extends the jet counting analysis at the 20 GeV jet p_{T} threshold. In the 1ℓ category only, a separate NN discriminant is trained in each jet slice with 8 or less jets, to discriminate the higgsino signal from the $t\bar{t}$ background. The full distribution of the NN output, binned in four even bins with approximately equal signal fraction, is fitted in each of the regions with at least one b-jet. The NN training is performed imposing the constraint that the NN output distribution of the $t\bar{t}$ background be invariant with respect to the b-jet multiplicity. This property is later exploited in order to estimate the background from data, as described in Section 7. The invariance of the NN output with respect to the b-jet multiplicity is achieved with a distance correlation training [122]. The NNs are trained on a mixture of higgsino samples as signal, and $t\bar{t}$ as the only background.

The NN discriminant is constructed from a combination of low-level and high-level inputs. The low-level variables considered are the jet and leading lepton momenta, the individual pseudo-continuous b-jet score [108] of all jets, and the $E_{\text{T}}^{\text{miss}}$ magnitude and direction. The high-level inputs correspond to the jet and b-jet multiplicity of the event, minimum distance between the leading lepton and any jet, scalar p_{T} sum of all jets (H_T), scalar p_{T} sum of all b-jets, invariant mass of the three-jet system with highest system p_{T}, invariant mass of the $3\text{j} + \ell + \mathbf{p}^{\text{miss}}$ system with highest system p_{T} (assuming that the z-component of the missing momentum $\mathbf{p}^{\text{miss}}$ is zero), and m^{jets} which is defined as follows. All the jets in the event are split into two groups, where both groups have to contain at least one jet. All possible combinations are tested, including those where the number of jets in each group is very different. For each grouping, the higher of the masses of the two groups is selected, and then the minimum across all possible groupings is taken. The m^{jets} distribution has an endpoint for signal events at $m(\tilde{\chi}_1^0)$ that is reached in events where all partons were reconstructed. For most events, the value is lower, since the lepton and $E_{\mathrm{T}}^{\mathrm{miss}}$ components are ignored. Backgrounds however do not show such an endpoint. In addition, the shape of this variable has only a weak dependence with respect to the number of b-jets, which helps the NN in achieving separation while not introducing sensitivity on the b-jet multiplicity.

The inputs are connected to a single output node via two fully connected hidden layers of 100 neurons. The NNs are trained using PyTorch [123] and the Adam optimiser [124]. Events in the training dataset are sampled according to the inverse of the b-jet fraction in order to flatten the b-jet spectrum. In order to achieve invariance of the NN output with respect to the b-jet multiplicity, the loss function of the training contains a term that penalises a high distance correlation between the output and the b-jet multiplicity. A hyperparameter λ controls the weight of this penalty term, with a value $\lambda = 15$ which was optimised to achieve the highest sensitivity to the signal, accounting for both the separation and the systematics derived from non-invariance of the NN, as described in Section 8. The invariance and separation achieved is shown in Figure 2. After training, the highest ranked variables according to their importance (using the integrated gradients method described in Ref. [125]) are H_T, the individual pseudo-continuous b-jet score of all jets, number of b-jets, invariant mass of the $3\mathrm{j} + \ell + \mathbf{p}^{\mathrm{miss}}$ system with highest system p_{T}, and m^{jets}. The b-jet multiplicity is highly ranked despite the NN output being invariant to it since it can be used to offset the effect from variables that are correlated with the number of b-jets such as H_T.

In the $2\ell^{\mathrm{sc}}$ category signal events are produced via the leptonic decay of two top quarks. However, the dominant backgrounds contain only one leptonic top decay, while the second lepton is a misidentified or non-prompt lepton, or originates from a W that is not produced in a top decay ($t\bar{t}W$). This property is exploited by introducing an additional requirement of $m^{\ell j} < 155\,\mathrm{GeV}$, where the observable $m^{\ell j}$ is defined as $m^{\ell j} = \min_{a,b} \left\{\max\left(m(\ell_0, \mathrm{jet}_a), m(\ell_1, \mathrm{jet}_b)\right)\right\}$, with $\mathrm{jet}_a \neq \mathrm{jet}_b$, for all possible permutations of jet_a, jet_b taken from the four leading jets. No b-tag information is used in the selection of the jets to avoid differences in the variable across the different b-tag regions. The signal has an endpoint in this variable at $m^{\ell j} = \sqrt{m_{\mathrm{top}}^2 - m_W^2} \approx 152\,\mathrm{GeV}$, while background events tend to have larger values.

In order to probe a specific BSM model, all the regions in both lepton categories are simultaneously fit to data to constrain the model, in what is denoted as a model-dependent fit. Separate fits are performed for each analysis and jet p_{T} threshold. In the search for a generic BSM signal, dedicated discovery signal regions (SRs) are defined which could be populated by a signal, and where the SM contribution is expected to be small. The background in these SRs is estimated from a fit excluding the SR being tested, in what is denoted as a model-independent fit. The discovery SR definitions used in the jet counting analysis are shown in Table 3.

Two additional discovery SRs are defined targeting a possible electroweakino signal making use of the EWK analysis. The first SR is defined in the 1ℓ category, with exactly 6 jets with $p_{\mathrm{T}} > 20\,\mathrm{GeV}$, at least 4 b-jets, and a selection on the NN discriminant corresponding to a signal efficiency of 25% and a background rejection of 40 for the $t\bar{t}$ background, which corresponds to bin four in Figure 2. The second SR is defined in the $2\ell^{\mathrm{sc}}$ category, with exactly 6 jets with $p_{\mathrm{T}} > 20\,\mathrm{GeV}$, and at least 3 b-jets. The discovery SR definitions used in the EWK analysis are also shown in Table 3.

The dominant background processes are $t\bar{t}$+jets and W/Z+jets in the 1ℓ category, and $t\bar{t}W$, $t\bar{t}$ with a misidentified lepton, and diboson production in the $2\ell^{\mathrm{sc}}$ category. The estimation of the dominant backgrounds is carried out using a combined fit to the jet and b-jet multiplicity bins described above. For these backgrounds, the normalisation per jet slice is derived using parameterized extrapolations from lower jet multiplicities. The b-jet multiplicity shape per jet slice is taken from MC simulation for the W/Z+jets and diboson backgrounds, whereas for background processes involving top-quarks it is predicted from the

Jet counting analysis discovery SRs			
Jet p_{T} threshold	Number of jets 1ℓ category	Number of jets 2ℓ^{sc} category	Number of b-jets
20 GeV	≥ 15	≥ 10	$= 0, \geq 3$
40 GeV	≥ 12	≥ 8	$= 0, \geq 3$
60 GeV	≥ 11	≥ 7	$= 0, \geq 3$
80 GeV	≥ 10	≥ 7	$= 0, \geq 3$
100 GeV	≥ 8	≥ 6	$= 0, \geq 3$

EWK analysis discovery SRs			
Jet p_{T} threshold	Lepton category and selection	Number of jets	Number of b-jets
20 GeV	1ℓ, NN bin 4	$= 6$	≥ 4
20 GeV	2ℓ^{sc}, $m^{\ell j} < 155$ GeV	$= 6$	≥ 3

Table 3: The discovery signal regions used in jet counting and NN analyses, for the search of a generic BSM signal. For every jet p_{T} threshold four signal regions are defined in the jet counting analysis, leading to a total of 20 discovery signal regions defined in the jet counting analysis. Two additional discovery signal regions are defined in the EWK analysis.

data using a parameterized extrapolation based on observables at medium jet multiplicities. A separate likelihood fit is carried out for each jet p_{T} threshold, with the fit parameters of the background model determined separately in each fit. The assumptions used in the parameterization are validated using data and MC simulation.

7 Background estimation

The dominant background in the 1ℓ category arises from W/Z+jets production in the zero b-jet regions, and top-quark pair production in the regions with at least one b-jet. In the 2ℓ^{sc} category the dominant background in the zero b-jet regions originates from diboson production with fully leptonic decays, in particular WZ where one lepton from the Z boson decay is lost. In the regions with at least one b-jet the main backgrounds are the associated production of a top-quark pair and a W boson, dileptonic $t\bar{t}$ where an electron has its charge misidentified, as well as semileptonic $t\bar{t}$ with a jet misidentified as a lepton, or with a non-prompt lepton. These three background components are merged and labelled as $t\bar{t}X^{\mathrm{sc}}$, and estimated simultaneously.

The theoretical modelling of all these backgrounds at high jet multiplicity suffers from large uncertainties, so they are estimated from the data by extrapolating the jet and b-jet multiplicity distributions extracted at moderate jet multiplicities, to the high jet multiplicities of the search regions.

7.1 Jet multiplicity prediction

A data-driven approach is used to estimate contribution of the main backgrounds in each jet multiplicity slice. The estimate of the normalisation relies on assuming a functional form to describe the evolution of the number of background events for process X as a function of the jet multiplicity, $r^X(j) \equiv N^X_{j+1}/N^X_j$.

Above a certain number of jets, $r(j)$ can be assumed to be constant, implying a fixed probability of additional jet radiation, referred to as "staircase scaling" [126–129]. This behaviour has been observed in W/Z+jets by the ATLAS [130, 131] and CMS [132] collaborations. For lower jet multiplicities, a different scaling is expected with $r(j) = k/(j + 1)$ where k is a constant, referred to as "Poisson scaling" [129]. Note that the transition between these scaling behaviours depends on the jet kinematic selections.

For the kinematic phase space relevant for this search, a combination of the two scalings is found to describe the data in dedicated validation regions (described later in this section), as well as in simulated MC samples with an integrated luminosity much larger than that of the data. This combined scaling is parameterized as

$$r^X(j) = c^X_0 + c^X_1/(j + c^X_2), \tag{1}$$

where c^X_0, c^X_1 and c^X_2 are process-dependent constants that are extracted from the data. The c^X_2 parameter is introduced to take into account the ambiguity in the counting of jets originating from the decay of the process X and the additional jets. The parameter is fixed to $c^X_2 = 1$ in the estimation of W+jets, Z+jets, and fully leptonic diboson events, as there is no ambiguity in the counting of jets for these processes. However, c^X_2 is a free parameter in the estimation of backgrounds containing top-quarks, where the jet counting ambiguity remains.

Studies using simulated event samples, both at generator level and after event reconstruction, demonstrate that the flexibility of this parameterization is also able to absorb reconstruction effects related to the decrease in event reconstruction efficiency with increasing jet multiplicity, which are mainly due to the lepton–jet overlap and lepton isolation requirements.

The number of background events from process X in the j jets slice is then parameterized as follows:

$$N^X_j = N^X_4 \cdot \prod_{j'=4}^{j'=j-1} r^X(j'),$$

where N^X_4 is a free parameter for the absolute normalisation in four-jet events. Since the last jet-multiplicity bin used in the analysis is inclusive in the number of jets, the model is used to predict this by iterating to higher jet multiplicities and summing the contribution for each jet multiplicity above the maximum used in the analysis. The four parameters per process N^X_4, c^X_0, c^X_1, and c^X_2 (if not fixed to one) are left floating in the fit, and are therefore extracted from the data along with the other background contributions. Studies in data and MC simulation indicate that the c^X_0, c^X_1 parameters for W+jets and Z+jets are statistically compatible, and are therefore combined into common parameters $c_0^{W/Z\text{+jets}}$, $c_1^{W/Z\text{+jets}}$. The normalisation parameters $N_4^{W\text{+jets}}$ and $N_4^{Z\text{+jets}}$ are kept independent. The c^X_i parameters are independent among the rest of the backgrounds, including $t\bar{t}$ in the 1ℓ category and $t\bar{t}X^{\text{sc}}$ in the $2\ell^{\text{sc}}$ category.

The jet-scaling assumption is validated in data using γ+jets and dileptonic $t\bar{t}$ events. The γ+jets events are selected using a high p_{T} photon trigger, and a signal high p_{T} photon is required in the event selection. The dileptonic $t\bar{t}$ data sample is selected by requiring an electron candidate and a muon candidate in the event, with at least two jets of which at least one is a b-jet, and the small background predicted by MC simulation

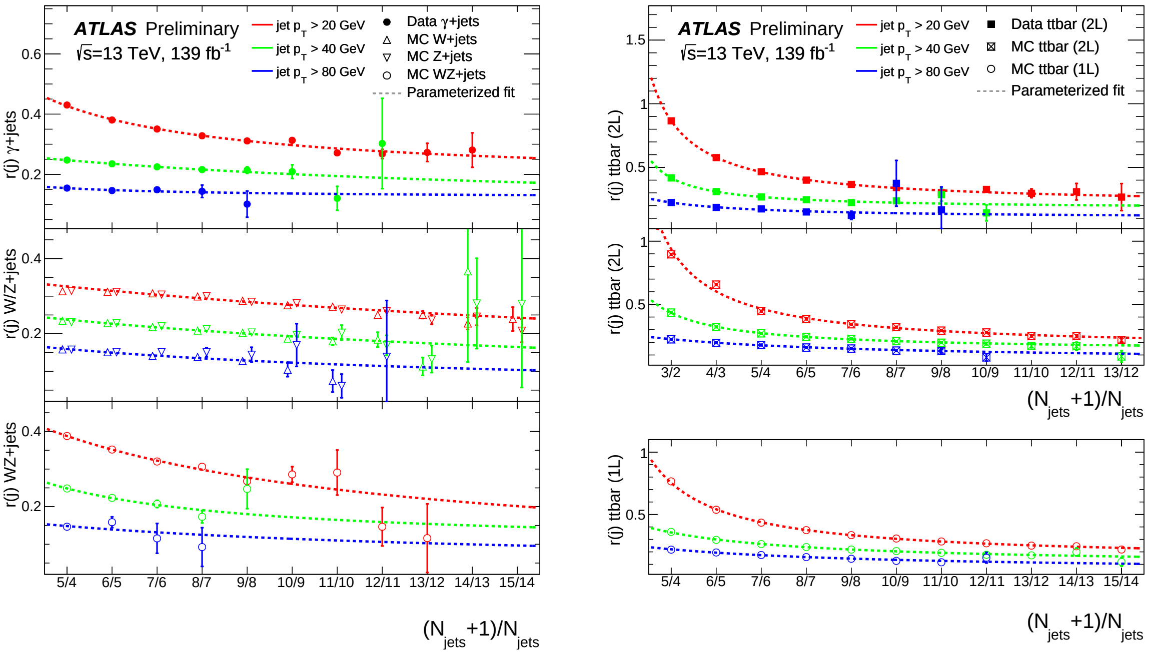

Figure 3: The ratio of the number of events with $(j + 1)$ jets to the number with j jets in various event samples (details in the legend), used to validate the jet-scaling parameterization. In the MC samples of $W/Z/WZ$+jets the vector bosons are forced to decay to leptons. Each panel shows the ratio for data or MC simulation with the fitted parameterization overlaid as a dashed line. The uncertainties shown are statistical.

is subtracted. In this sample, the scaling behaviour can be tested for up to thirteen jets, which corresponds to fifteen jets for a semileptonic $t\bar{t}$+jets sample. Simulated W+jets, Z+jets, semileptonic $t\bar{t}$ (both with the nominal sample and the alternative sample described in Section 4), and $t\bar{t}X^{\mathrm{sc}}$ samples are also found to be consistent with the jets-scaling assumption.

Figure 3 shows the $r(j)$ ratio for various processes used to validate the jet-scaling parameterization. Each panel shows the $r(j)$ ratio for data or MC simulation with the fitted parameterization overlaid as a line.

7.2 B-jet multiplicity prediction

The number of background events from process X in a given jet and b-jet multiplicity region can be expressed as follows:

$$N^X_{j,b} = f^X_{j,b} \cdot N^X_j$$

where $f^X_{j,b}$ is the fraction of events from process X with b number of b-jets in the j jet slice, and satisfy $\sum_b f^X_{j,b} = 1$. A data-driven model is used to estimate the b-jet fraction in background processes containing top-quarks. The basic concept of this model is based on the extraction of an initial template of the b-jet fraction distribution in events with four jets and the parameterization of the evolution of this template to higher jet multiplicities. Each jet slice is constrained in the fit as discussed later in this section. The b-jet fractions for W+jets, Z+jets and diboson backgrounds are taken from MC simulation.

The extrapolation of the b-jet multiplicity distribution to higher jet multiplicities starts from the assumption that the difference between the b-jet multiplicity distribution in events with j and $j + 1$ jets arises mainly from the production of additional jets, and can be described by a fixed probability that the additional jet is a b-jet. Given the small mis-tag rate, this probability is dominated by the probability that the additional jet is a heavy-flavour jet which is b-tagged. In order to account for acceptance effects due to the different kinematics in events with high jet multiplicity, the probability of further b-tagged jets entering the acceptance is also taken into account. The extrapolation to one additional jet can be parameterized as:

$$f_{(j+1),b} = f_{j,b} \cdot x_0 + f_{j,(b-1)} \cdot x_1 + f_{j,(b-2)} \cdot x_2, \tag{2}$$

where the parameters x_i describe the probability of one additional jet to be either not b-tagged (x_0), b-tagged (x_1), or b-tagged and causing a second b-tagged jet to move into the fiducial acceptance (x_2). The latter is dominated by cases where the extra jet is a b-jet, influencing the event kinematics such that an additional b-jet, previously below the jet p_{T} threshold, enters the acceptance. Given that the x_i parameters describe probabilities, the sum $\sum_i x_i$ is normalised to unity. Subsequent application of this parameterization produces a b-jet template for arbitrarily high jet multiplicities.

Studies based on MC simulated events with sample sizes corresponding to equivalent luminosities much larger than the collected dataset, as well as studies using fully efficient generator-level b-tagging, indicate the necessity to add a fit parameter that allows for correlated production of two b-jets as may be expected with b-jet production from gluon splitting. This is implemented by changing the evolution described in Eq. (2) such that any term with $x_1 \cdot x_1$ is replaced by $x_1 \cdot x_1 \cdot \rho_{11}$, where ρ_{11} describes the correlated production of two b-jets. The value of ρ_{11} is a free parameter and is determined in the fit.

The initial b-jet multiplicity template is extracted from data events with four jets after subtracting all non-$t\bar{t}$ background processes, and is denoted by $f_{4,b}$ and scaled by the absolute normalisation $N_4^{t\bar{t}\text{+jets}}$ in order to obtain the model in the four-jet bin:

$$N_{4,b}^{t\bar{t}\text{+jets}} = N_4^{t\bar{t}\text{+jets}} \cdot f_{4,b},$$

where the sum of $f_{4,b}$ over the four b-jet bins is normalised to unity. The zero b-jet component of the initial $t\bar{t}$ template, exhibits an anti-correlation with the absolute W+jets normalisation, which is extracted in the same region. The division in sub-regions separated in leading-lepton charge, detailed in Section 6, provide a handle to extract the absolute W+jets normalisation. The remaining anti-correlation does not affect the total background estimate. For these regions, the $t\bar{t}$+jets process is assumed to be charge symmetric and the model is simply split into two halves for these bins.

The model described above is based on the assumption that any change of the b-jet multiplicity distribution is due to additional jet radiation with a certain probability to lead to b-jets. There is, however, also a small increase in the acceptance for b-jets produced in the decay of the $t\bar{t}$ system, when increasing the jet multiplicity, due to the higher jet momentum on average. The effect amounts to up to 5% in the one and two b-jet bins for high jet multiplicities, and is taken into account using a correction to the initial template extracted from simulated $t\bar{t}$ events.

The parameters that model the production of additional b-jets (x_i, ρ_{11}) are correlated in the 1ℓ and $2\ell^{\mathrm{sc}}$ categories. The initial b-jet multiplicity parameters ($f_{4,b}$), and the acceptance correction to the initial template are independent in each lepton category.

7.3 Neural network template prediction

The NN is only introduced in regions with at least one b-jet, where the dominant background is $t\bar{t}$ production. The NN output distribution is obtained from MC simulation for all the subdominant backgrounds. A

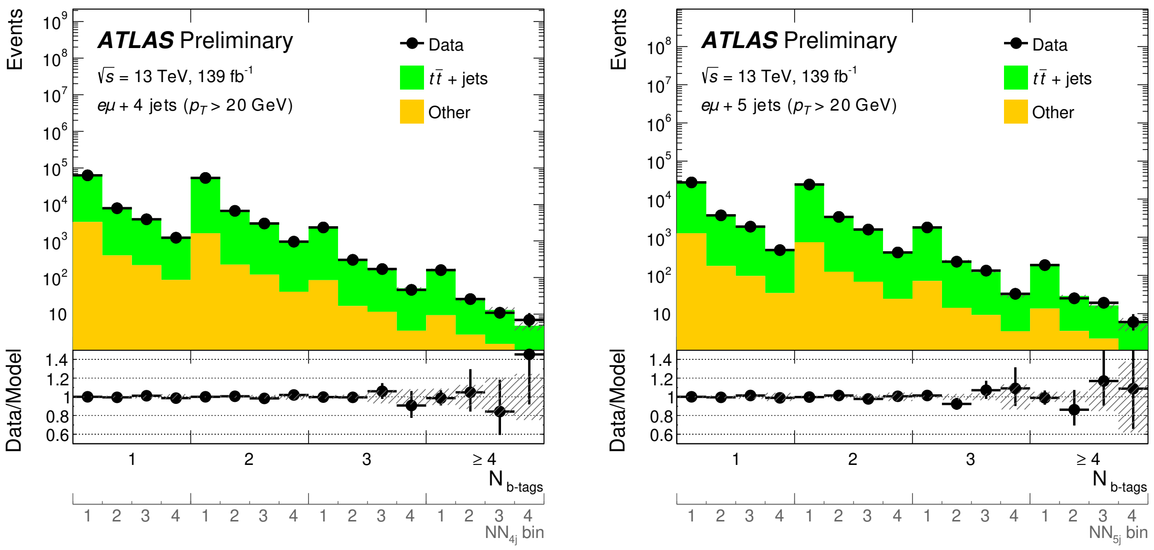

Figure 4: Observed data and the corresponding background estimation in regions with one electron, one muon, and four jets (left) or five jets (right). All uncertainties, which may be correlated across the bins, are included in the error bands (shaded regions). The shape of the NN template for the $t\bar{t}$ background is required to be identical in all b-jet regions. The good agreement between data and estimated background confirm the invariance of the NN output with respect to the b-jet region.

data-driven method is developed in order to predict the NN output distribution for $t\bar{t}$ background events, making use of the invariance of the NN output with respect to the number of b-jets in the event. The $t\bar{t}$ background in a given bin of the NN is parameterized as:

$$\mathrm{N}^{t\bar{t}\text{+jets}}_{j,b,i} = n_{j,i} \cdot N_{j,b}$$

where $n_{j,i}$ is the fraction of $t\bar{t}$ events in bin i of the NN in the j jet slice, and is independent of the b-jet region. The fractions in each jet slice are free parameters and are fitted simultaneously to all b-jet regions, respecting that the sum $\sum_i n^i_j$ is normalised to unity. Given the large statistical power of the one and two b-jet regions, the fitted NN templates are determined in these regions and not biased by a possible signal entering the high b-jet regions.

This method relies on the invariance of the NN output with respect to the number of b-jets. This property is validated in high-statistics samples of $t\bar{t}$ MC simulation, including the alternative samples described in Section 4. The invariance is also confirmed in data in a pure sample of dileptonic $t\bar{t}$ events, with a selection requiring one electron, one muon, and at least one b-jet. Figure 4 shows the good agreement between data and estimated background observed in this region, confirming in data the invariance of the NN output with respect to the b-jet region.

7.4 Fake and non-prompt lepton background

The contribution from backgrounds with a fake or non-prompt (FNP) lepton (such as hadrons misidentified as leptons, leptons originating from the decay of heavy-flavour hadrons, and electrons from photon conversions), constitutes a minor but non-negligible background.

The multijet background in the 1ℓ category is estimated from the data with a matrix method similar to that described in Ref. [133]. In this method, two types of lepton identification criteria are defined: *'tight'*, corresponding to the default signal lepton criteria described in Section 5, and *'loose'*, corresponding to candidate leptons after overlap removal. The matrix method relates the number of observed events in which a *loose* lepton candidate does or does not satisfy the *tight* selection criteria. The probability for *loose* prompt leptons to satisfy the *tight* selection criteria is obtained using a $Z \longrightarrow \ell\ell$ data sample and is modelled as a function of the lepton p_{T}. The probability for *loose* FNP leptons to satisfy the *tight* selection criteria is determined from a data control region enriched in non-prompt leptons requiring a *loose* lepton, multiple jets, low $E_{\mathrm{T}}^{\mathrm{miss}}$ [134, 135], and low transverse mass.[4] This data sample is recorded with prescaled lepton triggers without isolation requirement. The efficiencies are measured as a function of lepton candidate p_{T} after subtracting the contribution from prompt-lepton processes, and are assumed to be independent of the jet multiplicity.[5]

In the $2\ell^{\mathrm{sc}}$ category, the background from FNP leptons in association with a top-quark pair is estimated as part of the $t\bar{t}X^{\mathrm{sc}}$ background as described above. Other contributions from FNP leptons constitute less than 10% of the total background in the zero b-jet bin, with a negligible contribution in the b-jet regions, and are taken from MC simulation. A validation of the estimation is performed in a dedicated validation region requiring zero b-jets, two same-flavour leptons satisfying $|m_{ll} - m_Z| < 10\,\mathrm{GeV}$, and an additional candidate lepton failing the signal requirement. This region is dominated by Z boson events containing a FNP lepton, and is used to verify the modelling of FNP leptons in the MC simulation.

7.5 Minor backgrounds

The minor background contributions from single-top production, $t\bar{t}H$, and SM four-top-quark production are estimated using MC simulation. In the 1ℓ category the diboson and $t\bar{t}V$ backgrounds are also estimated from MC simulation, while they are both data-driven ($t\bar{t}V$ as part of the $t\bar{t}X^{\mathrm{sc}}$ background) in the $2\ell^{\mathrm{sc}}$ category. In all but the highest jet slices considered, the sum of these backgrounds contributes not more than 10% of the SM expectation in any of the b-jet bins; for the highest jet slices this can rise up to 35%.

7.6 Fit configuration and validation

Two different fit configurations are used in the search. When testing a specific BSM model the model-dependent fit setup is used, where all the regions in both lepton categories are simultaneously fit to data to constrain the model. The expected signal contribution in all bins is taken into account, including low jet and b-jet multiplicity bins. In the search for a generic BSM signal in a particular SR the model-independent fit setup is used, where all the regions are simultaneously fit excluding the SR being tested. Possible signal leakage to the control regions can produce a bias in the background estimation, leading to conservative limits. Such limits have been hence obtained assuming negligible signal contributions in regions outside of the SR. Signal processes with final states that the search is targeting, generally have negligible leakage into these regions, as is the case for the benchmark models considered.

The number of freely floating parameters in the background model is 26 in the jet counting analysis, and 41 in the EWK analysis. The different parameters for each background are summarised in Table 4. The

---

[4] The transverse mass of the lepton–$E_{\mathrm{T}}^{\mathrm{miss}}$ system is defined as: $m_{\mathrm{T}}^2 = 2p_{\mathrm{T}}^{\ell}E_{\mathrm{T}}^{\mathrm{miss}}(1 - \cos(\Delta\phi(\ell, E_{\mathrm{T}}^{\mathrm{miss}})))$.

[5] To minimise the dependence on the number of jets, the event selection considers only the leading-p_{T} candidate lepton when checking the more stringent identification and isolation criteria of the signal lepton definitions.

number of fitted bins varies between 51 and 110 in the jet counting analysis, depending on the jet p_{T} threshold used, and is 170 in the EWK analysis, leading to an over-constrained system in all cases.

The fit set-up was extensively tested using MC simulated events, and was demonstrated to give excellent agreement on a background-only dataset, and a negligible bias in the fitted signal yields. This agreement is seen both in the cases where the background-only distributions are fit, and when a signal is injected into the fitted data.

Parameters	$t\bar{t}$ +jets	$t\bar{t}X^{\mathrm{sc}}$	W+jets	Z+jets	VV+jets	Constraints
Normalisation	$N_4^{t\bar{t}}$	$N_4^{t\bar{t}X^{\mathrm{sc}}}$	N_4^W	N_4^Z	N_4^{VV}	–
Jet scaling, $i \in \{0, 1, 2\}$	$c_i^{t\bar{t}}$	$c_i^{t\bar{t}X^{\mathrm{sc}}}$	$c_i^{W/Z}$		c_i^{VV}	$c_2^{W/Z} = c_2^{VV} = 1$
Initial b-jet fractions, $i \in \{0 \dots 4\}$	$f_{4,i}^{t\bar{t}}$	$f_{4,i}^{t\bar{t}X^{\mathrm{sc}}}$	–	–	–	$\sum_i f_{4,i} = 1$
Extra heavy-flavour jets, $i \in \{0, 1, 2\}$	x_i, ρ_{11}		–	–	–	$\sum_i x_i = 1$
NN shape, $i \in \{1 \dots 4\}$, $j \in \{4 \dots 8\}$	$n_{j,i}$	–	–	–	–	$\sum_i n_{j,i} = 1$

Table 4: Summary of all the free floating parameters in the background model. There are a total of 26 such parameters in the jet counting analysis and 41 in the EWK analysis.

8 Systematic uncertainties

The dominant backgrounds are estimated from the data without the use of MC simulation, and therefore the main systematic uncertainties related to the estimation of these backgrounds arise from the assumptions made in the construction of the parameterized model. Uncertainties related to the theoretical modelling of the specific processes and due to the modelling of the detector response in simulated events are only relevant for the minor backgrounds, which are taken from MC simulation, and for the estimates of the signal yields after selections.

For the W/Z+jets background estimation, the uncertainty related to the assumed jet scaling is taken from studies of this behaviour in W+jets and Z+jets MC simulation, as well as in γ+jets data control regions chosen to be kinematically similar to the search selection. Deviations from the assumed scaling behaviour are assigned as a systematic uncertainty in each jet slice, or as the statistical precision of the validation in case of no deviation. The uncertainty in the lower jet multiplicities is at the percent level for all jet p_{T} thresholds, and up to 50% in the highest jet multiplicities, driven by the statistical precision of the method. The uncertainty related to the parameterization of the jet multiplicity of the $t\bar{t}$ background is determined with the same strategy, and is derived from MC simulation closure tests (including alternative MC generators), as well as dileptonic $t\bar{t}$ control regions in data. No evidence is seen for a deviation from the assumed scaling behaviour, and the statistical precision of the closure in data is used as an uncertainty.

The expected uncertainty of the charge asymmetry for W+jets production is 3–5% from PDF variations [136], but in the seven-jet region, the uncertainty is dominated by the limited number of MC events (up to 10% for the 80 GeV jet p_{T} threshold). The uncertainty in the shape of the b-jet multiplicity distribution in W+jets, Z+jets, and diboson events is derived by comparing different MC generator configurations (e.g. varying the renormalization and factorisation scale and the parton-shower model parameters). It is seen to grow as a function of jet multiplicity and is about 50% for events with five jets, after which the MC statistical uncertainty becomes very large. A conservative uncertainty of 50% per additional heavy flavour quark that is generated is assigned to the fractional contribution from $V(V)$+b and $V(V)$+c events, uncorrelated among the three backgrounds. This uncertainty has a negligible impact on the final result as the background from W/Z boson or diboson production with additional heavy flavour jets is small compared to that from top-quark pair production. In addition, the uncertainties related to the b-tagging efficiency and mis-tag rate are taken into account in the uncertainty in the W/Z+jets b-jet template.

The b-jet fraction estimation method exhibits good closure in studies based on MC simulated events with sample sizes corresponding to equivalent luminosities much larger than the collected dataset, as well as studies using fully efficient generator-level b-tagging, so no systematic uncertainty related to these studies is assigned. There is a small uncertainty related to the acceptance correction for the initial b-jet multiplicity template, which is derived by varying the MC generator configuration for the $t\bar{t}$ sample used to estimate the correction. This leads to a 3% uncertainty in the correction, and has no significant effect on the final uncertainty.

The prediction of the NN template in $t\bar{t}$ events relies on the invariance of the NN output with respect to the number of b-jets in the event. This assumption is tested in MC simulation and seen to hold within 5% in the 5 jet and 6 jet slices, where the best signal-to-background ratio is expected, and within 10% in the rest. The largest deviation per bin seen across b-jet regions from the b-jet-inclusive template is assigned as an uncorrelated uncertainty in each bin, which ranges from 1% to 10%.

The dominant uncertainties in the multi-jet background estimate arise from the number of data events in the control regions, uncertainties related to the subtraction of electroweak backgrounds from these control regions (here a 20% uncertainty is applied to the expected yield of the subtracted electroweak backgrounds), and uncertainties to cover the possible dependencies of the prompt and FNP lepton efficiencies [133] on variables other than lepton p_{T} (for example the dependence on the number of jets in the event). The total uncertainty in the multi-jet background yields is about 50%.

The uncertainty in the expected yields of the minor backgrounds includes theoretical uncertainties in the cross-sections and in the modelling of the kinematics by the MC generator, as well as experimental uncertainties related to the modelling of the detector response in the simulation. The uncertainties assigned to cover the theoretical estimate of these backgrounds in the relevant regions are 50% for diboson in the 1ℓ category and single top-quark production, and 30% for $t\bar{t}V/H$ production. An additional uncertainty of 50% is assigned to the contribution from $t\bar{t}V + b$ and $t\bar{t}V + c$ events These uncertainties are conservative estimates based on the impact seen from renormalization and factorisation scale variations, PDF variations, and comparisons with samples with an alternative parton shower model.

Uncertainties on the modelling of $t\bar{t}t\bar{t}$ are assigned from renormalization and factorisation scale variations, as well as from a comparison with simulated samples with an alternative parton shower model. An uncertainty of 100% on the cross-section is assigned to cover the range from the predicted to the measured cross-section [33]. Using instead the central value and the uncertainty from the ATLAS measurement leads to a 1% degradation in expected sensitivity.

The final uncertainty in the background estimate in the SRs is dominated by the uncertainty on the fitted model parameters, which stems from the statistical uncertainty of data events in the different jet slices. Systematic uncertainties do not contribute significantly in the jet counting analysis, and cause only a 1% loss in sensitivity. The systematic uncertainty related to the NN invariance is the leading systematic in the EWK analysis, causing a 30% loss in sensitivity, while other systematic uncertainties are subdominant.

The uncertainties assigned to the expected signal yield for the SUSY benchmark processes considered include the experimental uncertainties related to the detector modelling, which are dominated by the modelling of the jet energy scale, and the b-tagging efficiencies and mis-tagging rates. For example, for a signal model with four b-quarks, the b-tagging uncertainties are $\approx$10%, and the jet related uncertainties are typically $\approx$5%. The uncertainty in the signal cross-sections used is discussed in Section 4. The uncertainty in the signal yields related to the modelling of additional jet radiation is studied by varying the factorisation, renormalization, and jet-matching scales as well as the parton-shower tune in the simulation. The corresponding uncertainty is small for most of the signal parameter space, but increases to up to 30% for very light or very heavy LSPs where the contribution from additional jet radiation is relevant.

9 Results

Results are provided both as model-independent limits on the contribution from BSM physics to the dedicated SRs, and in the context of the five SUSY benchmark models discussed in Section 2. As described in Section 6, two different fit configurations are used for the two sets of results. In both cases, the profile likelihood-ratio test [137] is used to establish 95% confidence intervals using the $\mathrm{CL_s}$ prescription [138]. The parameter of interest is the signal strength, defined as the cross-section of the hypothetical contribution from physics beyond the SM in unit of the cross-section of the benchmark model.

The b-jet multiplicity distributions are shown in Figures 5 and 6 for the EWK analysis defined with 20 GeV jet p_{T} threshold, for the 1ℓ and $2\ell^{\mathrm{sc}}$ categories. Figure 7 summarises the observed pulls in all analysis regions, defined as the difference between the observed number of events and the total number of expected events determined by the fit divided by the total uncertainty. The total uncertainty is the sum in quadrature of the statistical error of the observed data and the uncertainty on the predicted background. Figure 8 shows the b-jet multiplicity distribution for the last jet multiplicity bin defined for each of the jet p_{T} thresholds, in both the 1ℓ and $2\ell^{\mathrm{sc}}$ categories, which contains the discovery SRs at zero b-jet, and high b-jet multiplicity. The likelihood fit is configured using the model-dependent configuration where all bins are input to the fit, and fixing the signal-strength parameter to zero.

9.1 Model-independent results

The observed data event yields and the corresponding estimates for the backgrounds in the discovery SRs defined for the 1ℓ and $2\ell^{\mathrm{sc}}$ categories are shown in Tables 5 and 6. For each SR a fit is performed to predict the background using the model-independent setup, which excludes the SR under consideration. In addition, the p_0-values and corresponding significance are shown, which quantify the probability that a background-only experiment results in a fluctuation giving an event yield equal to or larger than the one observed in the data. No significant excess of data over the expected event yields is observed in any of the SRs. The two largest excesses are observed in the 60 GeV, $\geq$ 11 jets, $\geq$ 3 b-jets SR defined for the 1ℓ category and in the 60 GeV, $\geq$ 7 jets, $\geq$ 3 b-jets SR defined for the $2\ell^{\mathrm{sc}}$ category, and both correspond to a significance of 1.3 standard deviations.

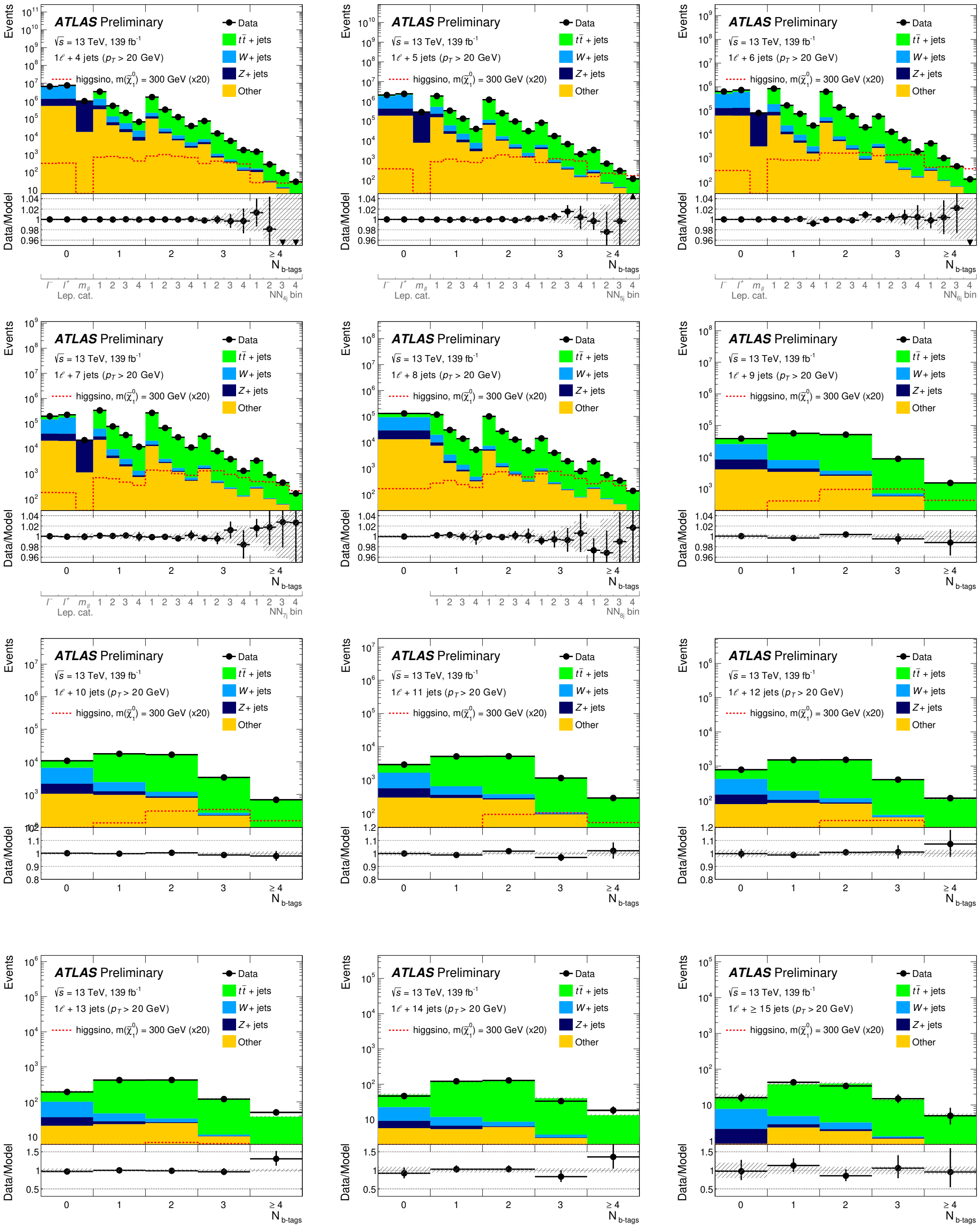

Figure 5: The observed data event yields and the corresponding estimates for the backgrounds in the different b-jet multiplicity bins for the 20 GeV jet p_{T} threshold regions defined for the EWK analysis in the 1ℓ category. The background shown is estimated by including all bins in the fit. All uncertainties, which may be correlated across the bins, are included in the error bands (shaded regions). The expected signal distribution for the higgsino LSP m($\tilde{\chi}_1^0$) = 300 GeV hypothesis is also overlaid.

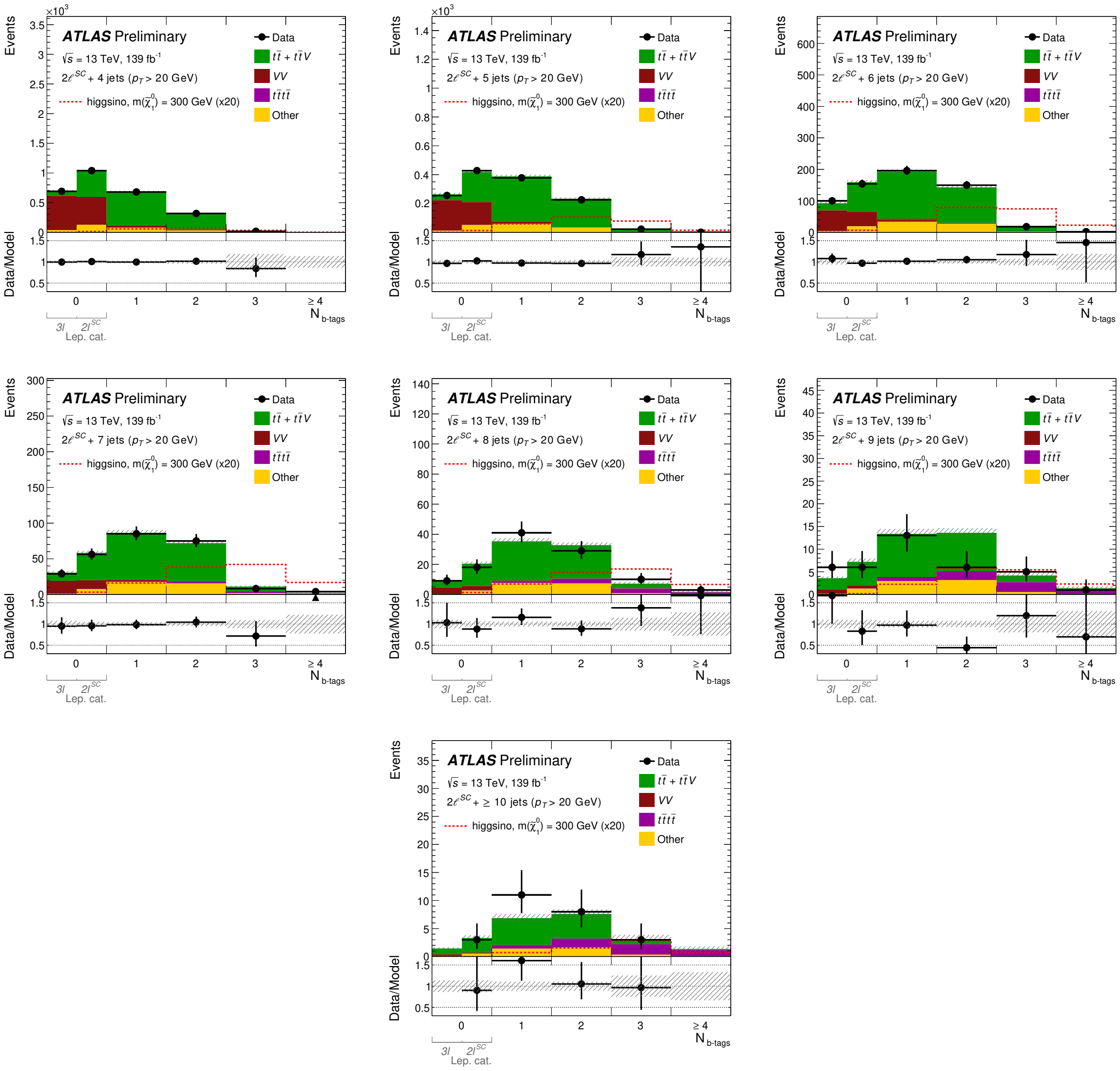

Figure 6: The observed data event yields and the corresponding estimates for the backgrounds in the different b-jet multiplicity bins for the 20 GeV jet p_{T} threshold regions defined for the EWK analysis in the $2\ell^{\mathrm{sc}}$ category. The background shown is estimated by including all bins in the fit. All uncertainties, which may be correlated across the bins, are included in the error bands (shaded regions). The expected signal distribution for the higgsino LSP m($\tilde{\chi}_1^0$) = 300 GeV hypothesis is also overlaid.

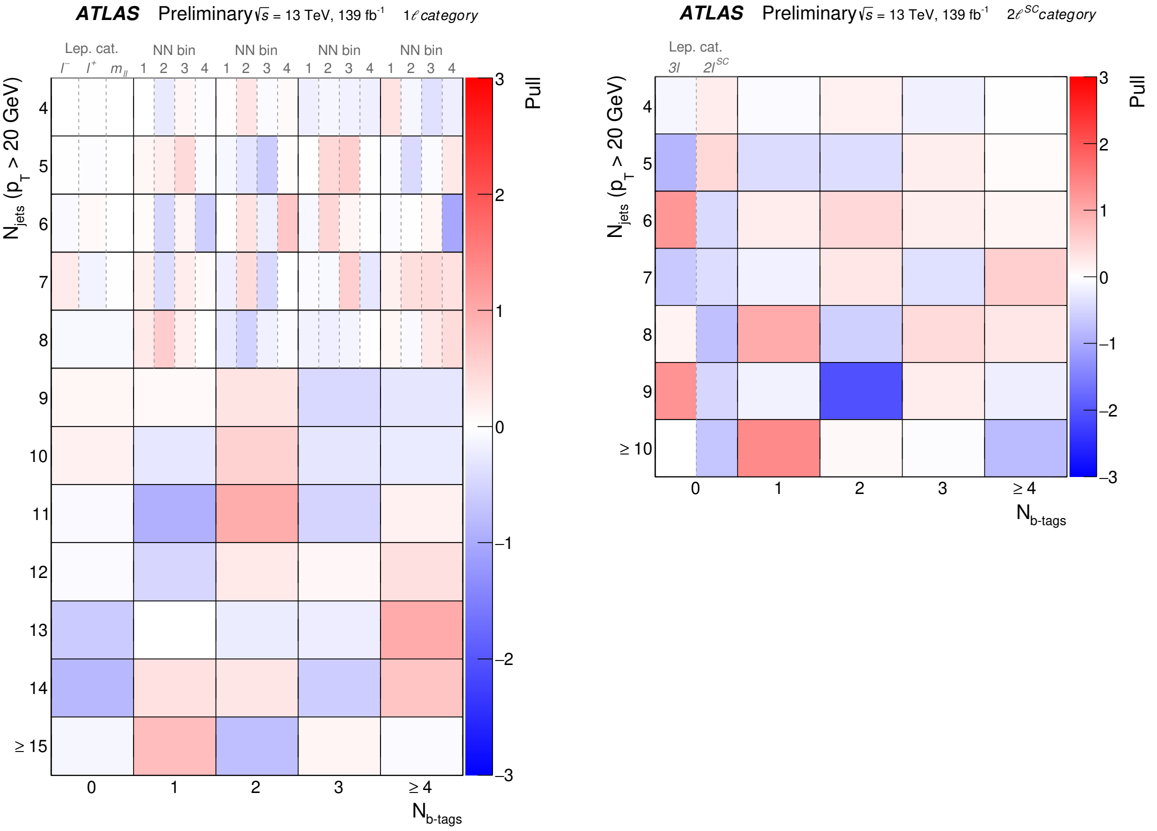

Figure 7: The observed pulls in all the regions considered in the EWK analysis, in the 1ℓ category (left) and the $2\ell^{\text{sc}}$ category (right). The pull is defined as the difference between the observed number of events and the total number of expected events determined by the fit divided by the total uncertainty. The total uncertainty is the sum in quadrature of the statistical error of the observed data and the uncertainty on the predicted background.

9.2 Model-dependent results

For each signal model probed, the fit is configured using the model-dependent configuration. The jet counting analysis is used in the models with strong production and the EWK analysis for the models with electroweakino production. Separate fits are performed for each jet p_{T} threshold, and the threshold with best expected sensitivity for the given signal mass point is used to set limits. Figure 9 shows the observed and expected exclusion limits for the strong production signal models featuring gluino and stop pair production, as a function of the gluino mass or stop mass. Gluino masses up to 2.4 TeV are excluded for high LSP masses, and up to 2 TeV for low LSP masses. Stop masses are excluded up to 1–1.3 TeV, depending on the LSP mass. The best sensitivity is achieved for a bino LSP, while the wino LSP exhibits the worst sensitivity due to the reduced number of top quarks in the final state. The exclusion limits for the models with gluino or stop production are improved with respect to the previous version of the analysis documented in Ref. [22], thanks to the larger dataset and the inclusion of the same-sign lepton category.

Figure 10 shows exclusion limits in the electroweakino pair production model, versus the LSP mass. The limit for pure higgsino and wino LSPs are shown separately, taking into account the processes discussed in Section 2. The wino signal can only contribute to the 1ℓ category, via $\tilde{\chi}_1^{\pm}\tilde{\chi}_1^0$ production, while the higgsino signal is also present in the $2\ell^{\text{sc}}$ category through $\tilde{\chi}_2^0\tilde{\chi}_1^0$ production. This leads to differences in

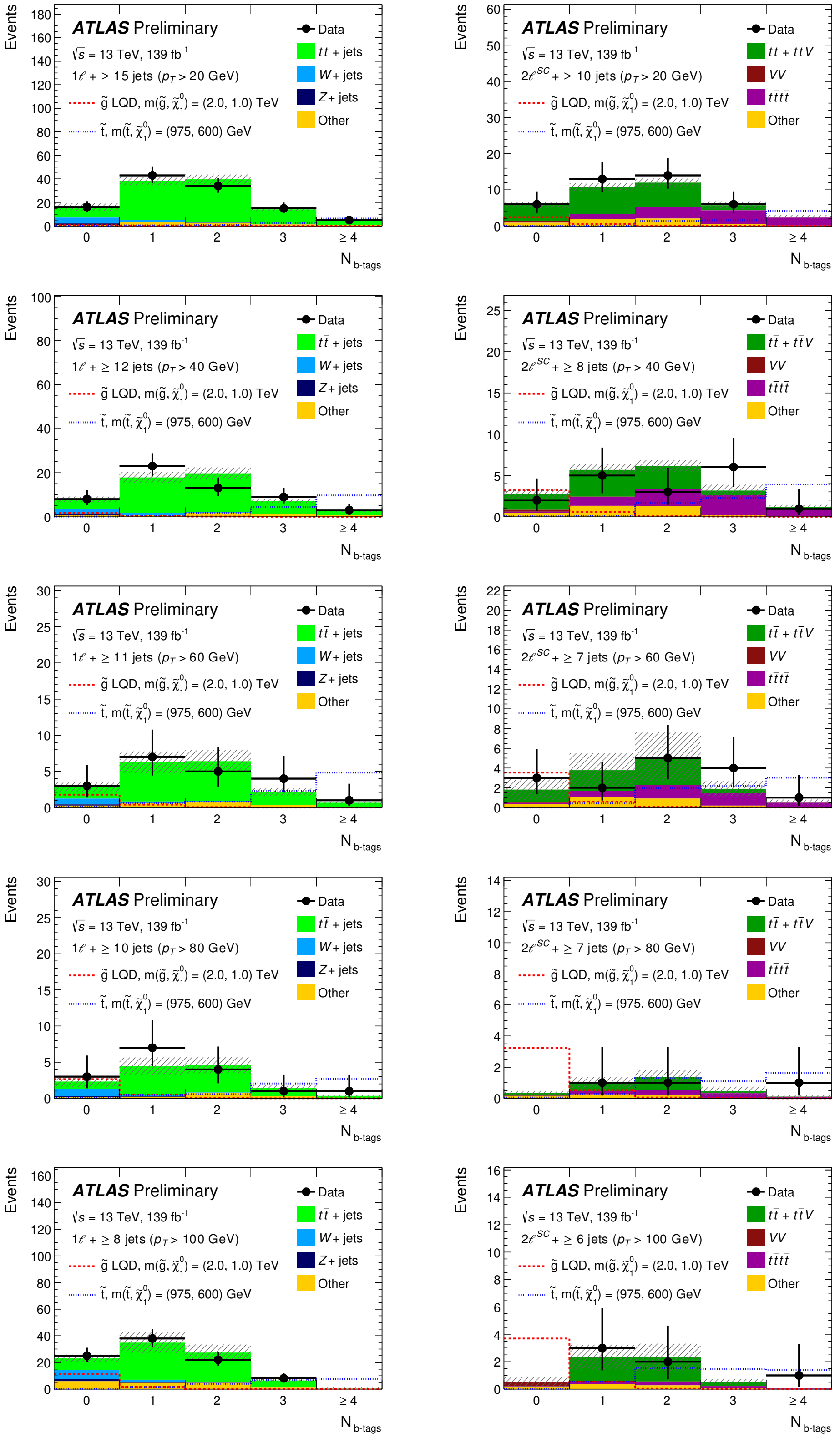

Figure 8: The observed data event yields and the corresponding estimates for the backgrounds in the different last jet multiplicity bin defined for the 1ℓ (left) and $2\ell^{\mathrm{sc}}$ (right) categories. The background shown is estimated by including all bins in the fit. All uncertainties, which may be correlated across the bins, are included in the error bands (shaded regions). Hypothetical contributions from representative RPV SUSY scenarios are displayed by the dashed-line.

Jet p_T threshold	Selection †=NN bin 4	Total background	Data	p_0	Z	σ^excl obs. [ab]	σ^excl exp. [ab]
20 GeV	$= 6j, \geq 4b$,†	145 ± 6	126	0.5	0	130	200^{+80}_{-60}
	$\geq 15j, = 0b$	16.3 ± 3.3	16	0.5	0	100	100^{+40}_{-30}
	$\geq 15j, \geq 3b$	17.0 ± 1.9	20	0.26	0.7	92	74^{+29}_{-21}
40 GeV	$\geq 12j, = 0b$	7.8 ± 1.5	8	0.47	0.1	55	53^{+21}_{-15}
	$\geq 12j, \geq 3b$	8.6 ± 1.1	12	0.17	0.9	76	55^{+21}_{-15}
60 GeV	$\geq 11j, = 0b$	2.7 ± 0.8	3	0.44	0.2	38	35^{+14}_{-10}
	$\geq 11j, \geq 3b$	2.3 ± 0.6	5	0.1	1.3	56	33^{+13}_{-9}
80 GeV	$\geq 10j, = 0b$	2.1 ± 1.1	3	0.38	0.3	42	34^{+13}_{-9}
	$\geq 10j, \geq 3b$	1.7 ± 1.5	2	0.47	0.1	35	33^{+13}_{-9}
100 GeV	$\geq 8j, = 0b$	22.7 ± 1.9	25	0.38	0.3	96	85^{+33}_{-24}
	$\geq 8j, \geq 3b$	7.5 ± 1.0	8	0.41	0.2	55	51^{+20}_{-14}

Table 5: Data event yields compared with the expected contributions from relevant background sources, in the discovery signal regions defined for the 1ℓ category. The p_0-value, and corresponding significance (Z), as well as the observed and expected 95% CL model-independent upper limits on product of cross-section, acceptance and efficiency (in ab) are also shown. In SRs with a deficit of data compared to the background prediction the p_0-value is capped at 0.5. The parameters of the model are determined in a fit to a reduced set of bins, corresponding to the model-independent fit discussed in the text.

the observed limits between both models. Depending on the LSP hypothesis, LSP masses between 200 (197) GeV and 320 (365) GeV are excluded for a higgsino (wino) LSP.

The analysis is also sensitive to SM $t\bar{t}t\bar{t}$ production, which produces a similar final state as the targeted signals. An additional model-dependent fit is performed where the $t\bar{t}t\bar{t}$ normalisation is a free parameter. The fitted normalisation of the four-top process relative to the Standard Model value is $\mu_{t\bar{t}t\bar{t}} = 2.0^{+0.9}_{-0.7}$. Modelling uncertainties due to scale variations and parton shower variation are taken into account, as well as a 20% cross-section uncertainty on the reference SM prediction of $\sigma_{t\bar{t}t\bar{t}}$ [91]. This is in agreement with the measured value in Ref. [33] of $\mu_{t\bar{t}t\bar{t}} = 2.0^{+0.8}_{-0.6}$. Both analyses are based on the same dataset and have overlapping selections, but have fully different background estimation methods. The best sensitivity is obtained with the 40 GeV jet p_T threshold. Compatible results, albeit with larger uncertainties, are obtained with the 20 GeV and 60 GeV jet p_T thresholds. A fit with two independent signal strengths in each lepton category yields consistent values in both categories.

Jet p_{T} threshold	Selection $\dagger = m^{\ell j} < 155$ GeV	Total background	Data	p_0	Z	σ^{excl} obs. [ab]	σ^{excl} exp. [ab]
20 GeV	$= 6j, \geq 3b, \dagger$	16.1 ± 1.2	20	0.21	0.8	92	69^{+27}_{-19}
	$\geq 10j, = 0b$	5.8 ± 0.8	6	0.46	0.1	48	45^{+18}_{-13}
	$\geq 10j, \geq 3b$	8.2 ± 1.5	6	0.5	0	41	54^{+21}_{-15}
40 GeV	$\geq 8j, = 0b$	2.8 ± 0.7	2	0.5	0	31	35^{+14}_{-10}
	$\geq 8j, \geq 3b$	3.6 ± 1.2	7	0.13	1.1	67	39^{+15}_{-11}
60 GeV	$\geq 7j, = 0b$	1.71 ± 0.35	3	0.2	0.8	41	29^{+12}_{-8}
	$\geq 7j, \geq 3b$	2.0 ± 0.7	5	0.09	1.3	58	32^{+13}_{-9}
80 GeV	$\geq 7j, = 0b$	0.34 ± 0.13	0	0.5	0	22	22^{+9}_{-0}
	$\geq 7j, \geq 3b$	0.54 ± 0.20	1	0.34	0.4	27	22^{+9}_{-0}
100 GeV	$\geq 6j, = 0b$	0.5 ± 0.4	0	0.5	0	22	22^{+9}_{-0}
	$\geq 6j, \geq 3b$	0.52 ± 0.22	1	0.28	0.6	28	22^{+9}_{-0}

Table 6: Data event yields compared with the expected contributions from relevant background sources, in the discovery signal regions defined for the $2\ell^{\mathrm{sc}}$ category. The p_0-value, and corresponding significance (Z), as well as the observed and expected 95% CL model-independent upper limits on product of cross-section, acceptance and efficiency (in ab) are also shown. In SRs with a deficit of data compared to the background prediction the p_0-value is capped at 0.5. The parameters of the model are determined in a fit to a reduced set of bins, corresponding to the model-independent fit discussed in the text.

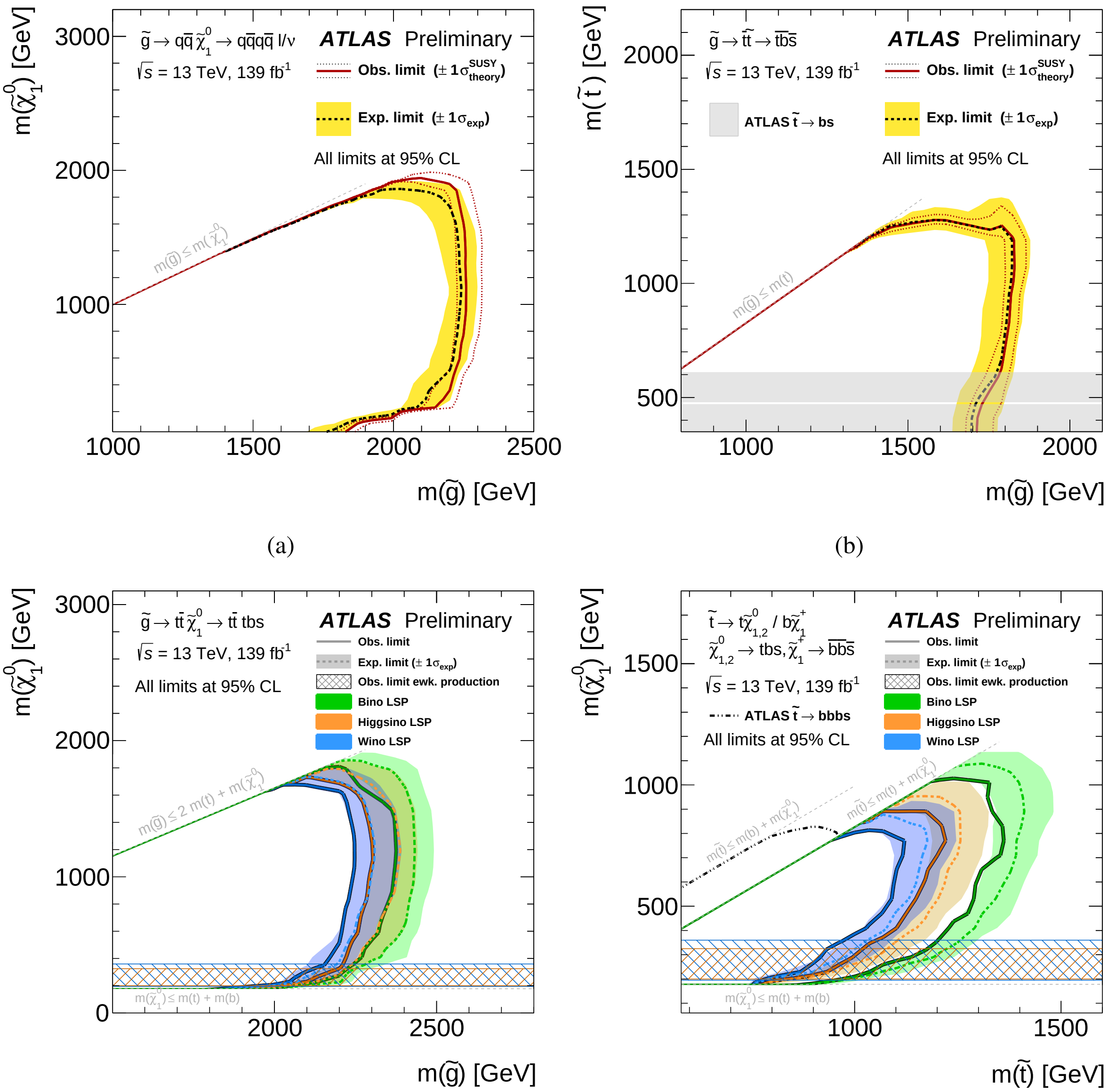

(a)

(b)

(c)

(d)

Figure 9: Observed and expected exclusion contours for the RPV models with strong production. The results are shown for (a) $\tilde{g} \rightarrow q\bar{q}\tilde{\chi}_1^0 \rightarrow q\bar{q}q\bar{q}\ell\nu$, (b) $\tilde{g} \rightarrow \bar{t}\tilde{t} \rightarrow \bar{t}\bar{b}\bar{s}$, (c) $\tilde{g} \rightarrow t\bar{t}\tilde{\chi}_1^0 \rightarrow t\bar{t}tbs/\tilde{g} \rightarrow t\bar{b}\tilde{\chi}_1^0 \rightarrow t\bar{b}bbs$ and (d) stop pair production. The $\tilde{g} \rightarrow t\bar{t}\tilde{\chi}_1^0 \rightarrow t\bar{t}tbs$ and stop exclusion limit plots also include the observed lines from direct electroweakino production obtained with the EWK analysis. The contours of the band around the expected limit are the $\pm 1\sigma$ variations, including all uncertainties. The dotted lines around the observed limit illustrate the change in the observed limit as the nominal signal cross-section is scaled up and down by the theoretical uncertainty. All limits are computed at 95% CL. The diagonal line indicates the kinematic limit for the decays in each specified scenario. The limits on direct electroweakino production obtained with the EWK analysis are displayed as horizontal hatched bands in (c) and (d). When relevant, the limit on the stop mass from Refs. [23, 27] are also shown. A small range in stop mass between 460 GeV and 470 GeV is not excluded by the search for $\tilde{t} \rightarrow bs$ [27].

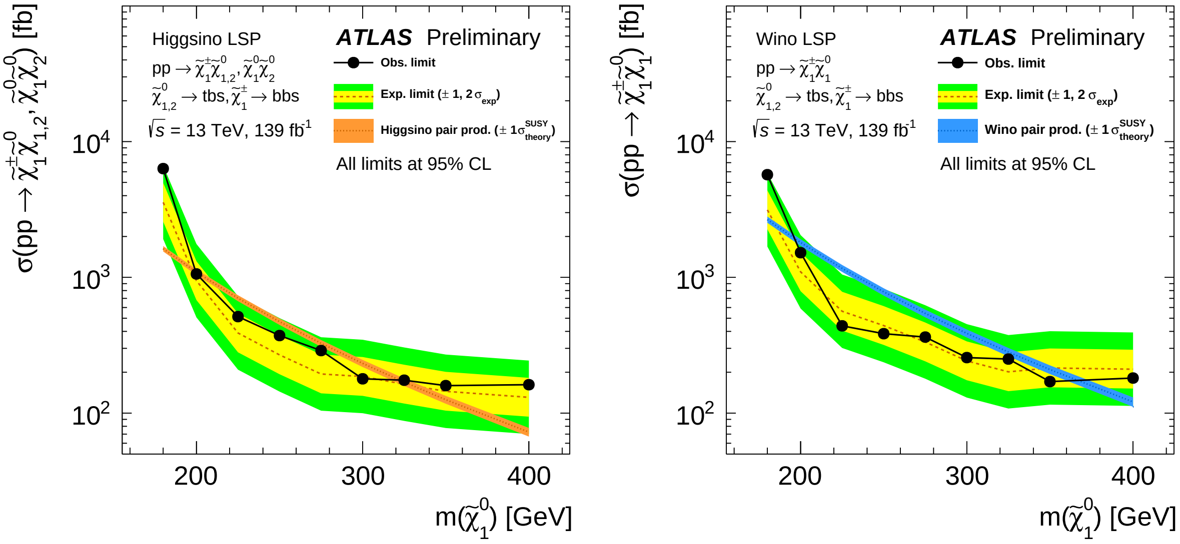

(a) (b)

Figure 10: Observed and expected exclusion contours for the RPV models with electroweakino production models with (a) higgsino and (b) wino LSP hypotheses. The yellow and green contours of the band around the expected limit are the $\pm 1\sigma$ and $\pm 2\sigma$ variations including all uncertainties, respectively. The theoretical prediction is also shown, with the uncertainties on the prediction shown as a coloured band. The production of $\tilde{\chi}_1^{\pm}\tilde{\chi}_1^{\pm}$ is not considered as it decays to a final state with no leptons.

10 Conclusion

A search for R-parity violating supersymmetry events with at least one isolated lepton (electron or muon) and high jet multiplicity is presented. In order to improve the sensitivity of the search, events with two leptons with same electric charge, and events with at least one lepton are analysed separately. The selection relies also on the number of b-jets in the event. In order to ensure the highest sensitivity to the electroweak production models, a neural network based analysis was introduced. Data-based techniques are used to estimate the dominant backgrounds from $t\bar{t}$+jets, W/Z+jets, diboson, and $t\bar{t}W$ production. The analysis is performed with proton–proton collision data at $\sqrt{s} = 13$ TeV collected from 2015 to 2018 with the ATLAS detector at the Large Hadron Collider corresponding to an integrated luminosity of 139 fb^{-1}.

With no significant excess over the Standard Model expectation observed, results are interpreted in the framework of simplified models featuring gluino, top-squark, or electroweakino pair production in R-parity-violating supersymmetry scenarios. In a benchmark model with $\tilde{g} \rightarrow t\bar{t}\tilde{\chi}_1^0 \rightarrow t\bar{t}tbs$, gluino masses up to 2.38 TeV are excluded at 95% confidence level. Top squarks with masses up to 1.36 TeV are excluded in a model with direct top-squark production and R-parity-violating decays of the LSP. In both models, three hypotheses for the LSP are tested: pure bino, pure wino, and pure higgsino. In a model with $\tilde{g} \rightarrow \bar{t}\tilde{t}$ and $\tilde{t} \rightarrow \bar{b}\bar{s}$, gluino masses up to 1.83 TeV are excluded, whereas in a model with $\tilde{g} \rightarrow q\bar{q}\tilde{\chi}_1^0 \rightarrow q\bar{q}q\bar{q}\ell/\nu$, gluino masses up to 2.25 TeV are excluded. Direct electroweak production of electroweakinos is also tested, and higgsino (wino) masses between 200 (197) GeV and 320 (365) GeV are excluded.

These results improve the previously existing LHC limits for the gluino and stop production models considered, owing to the larger luminosity, the dedicated categorisation and analysis of same electric charge lepton events, as well as the introduction of multivariate discriminants. The results on the electroweak production model also improve the limits on hadronic RPV decays of electroweakinos from LEP [139–141]. Model-independent limits are also set on the contribution of new phenomena to the signal-region yields.

Appendix

10.1 Event displays

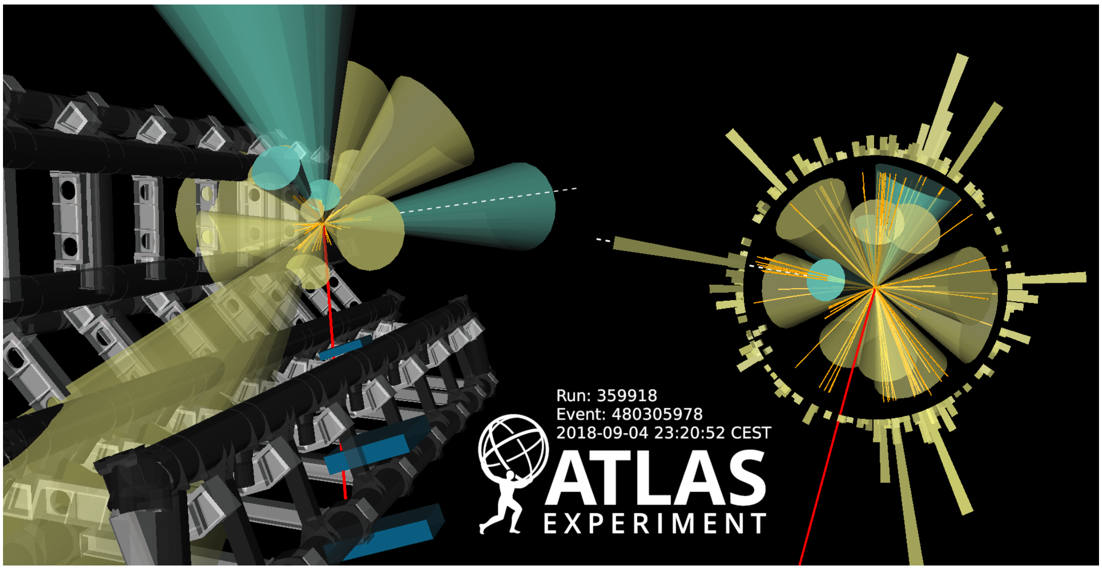

Figure 11: Display of an event containing one muon and multiple jets. The signal muon is indicated by the red line, and has $p_{\mathrm{T}} = 53$ GeV. There are 15 jets in this event, with p_{T} from 21 GeV to 182 GeV. Among these jets, 4 are b-jets, which are shown with a cyan cone and have p_{T} from 29 GeV to 137 GeV. The $E_{\mathrm{T}}^{\mathrm{miss}}$ has a value of 67 GeV and is indicated by the dotted white line.

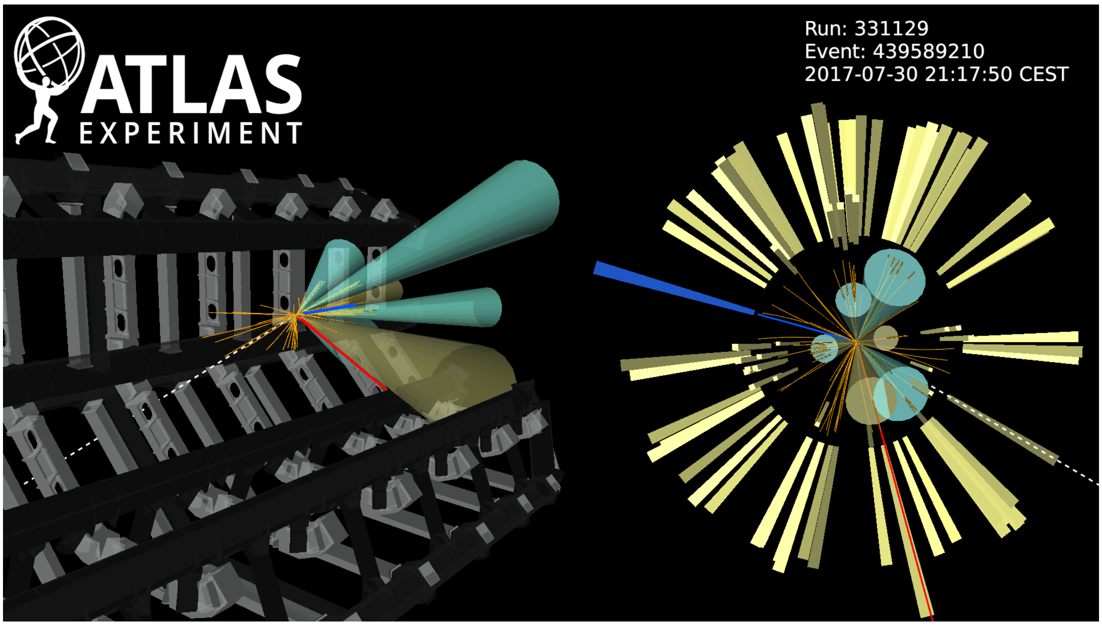

Figure 12: Display of an event from the higgsino signal region, containing a muon and electron with same electric charge, and 6 jets. The signal muon is indicated by the red line, and has $p_{\mathrm{T}} = 35$ GeV. The signal electron is indicated by the blue line, and has $p_{\mathrm{T}} = 61$ GeV. There are 6 jets in this event, with p_{T} from 41 GeV to 145 GeV. Among these jets, 4 are b-jets, which are shown with a cyan cone. The $E_{\mathrm{T}}^{\mathrm{miss}}$ has a value of 31 GeV and is indicated by the dotted white line.

10.2 Pulls

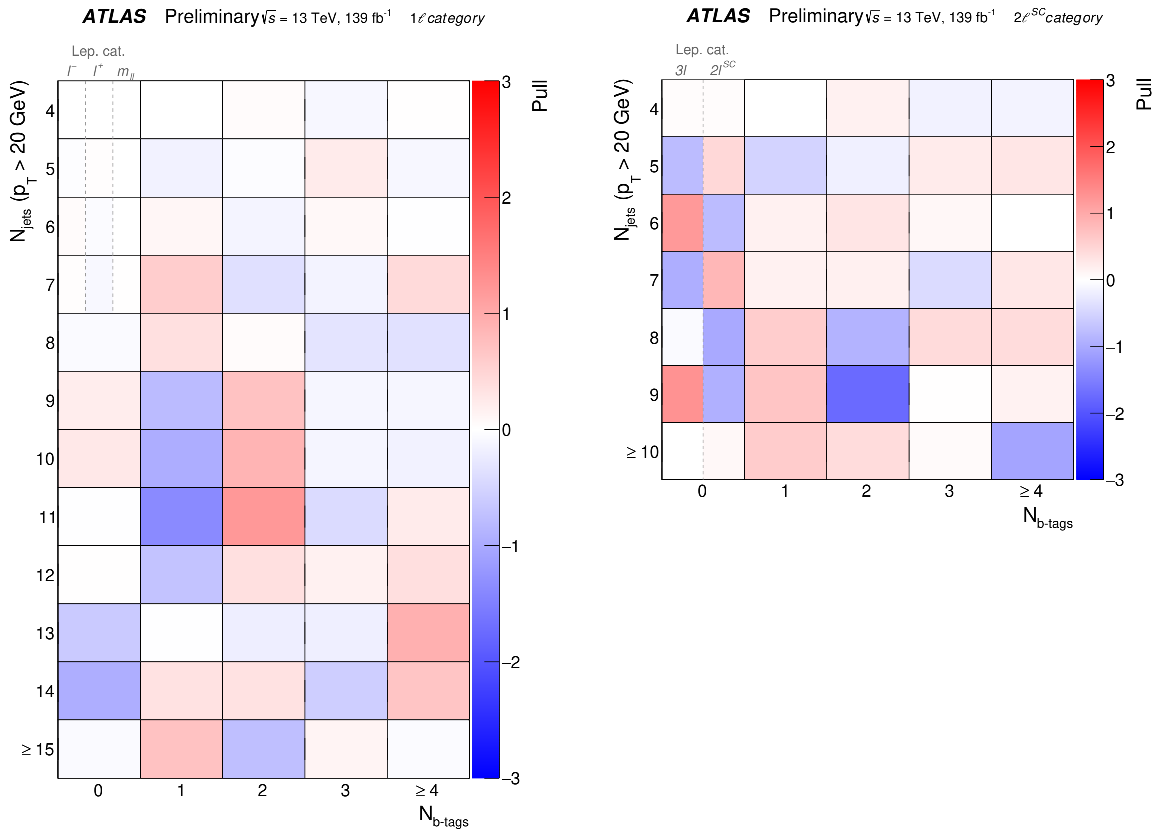

Figure 13: The observed pulls in all the regions considered in the jet counting analysis with 20 GeV jet p_T threshold, in the 1ℓ category (left) and the $2\ell^{sc}$ category (right). The pull is defined as the difference between the observed number of events and the total number of expected events determined by the fit divided by the total uncertainty. The total uncertainty is the sum in quadrature of the statistical error of the observed data and the uncertainty on the predicted background.

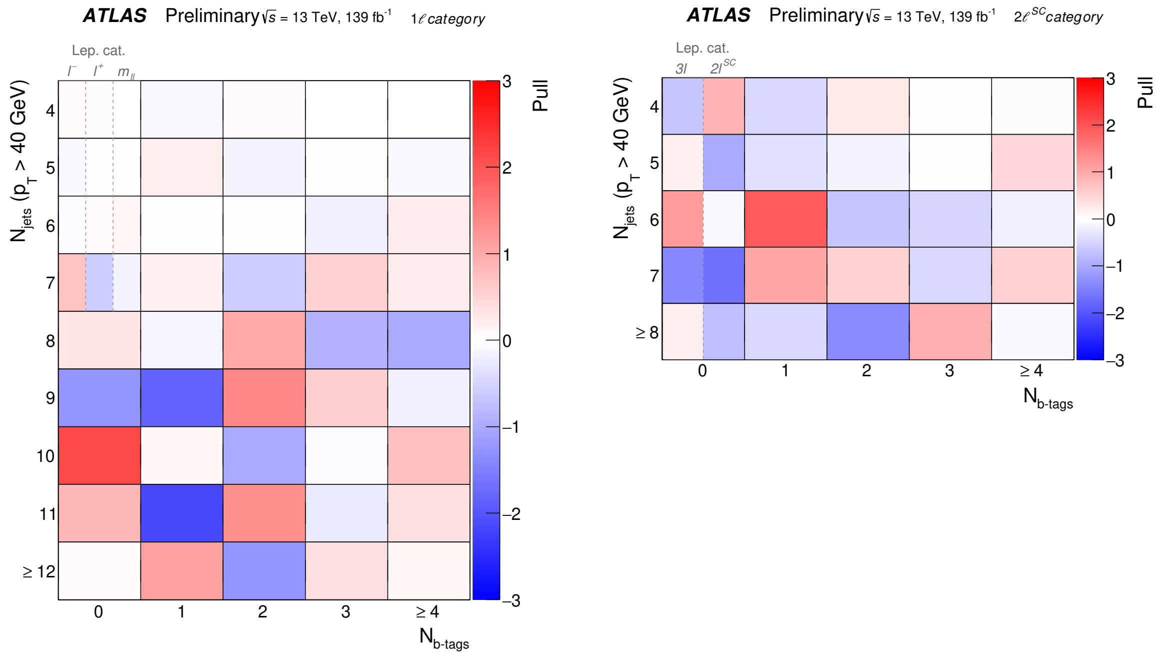

Figure 14: The observed pulls in all the regions considered in the jet counting analysis with 40 GeV jet p_T threshold, in the 1ℓ category (left) and the $2\ell^{sc}$ category (right). The pull is defined as the difference between the observed number of events and the total number of expected events determined by the fit divided by the total uncertainty. The total uncertainty is the sum in quadrature of the statistical error of the observed data and the uncertainty on the predicted background.

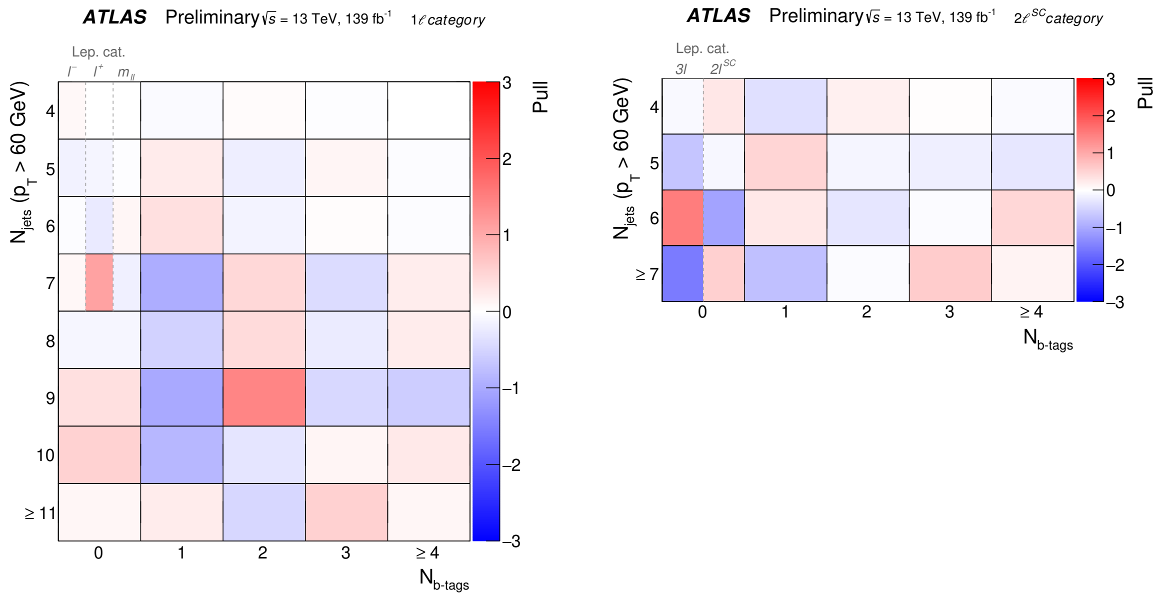

Figure 15: The observed pulls in all the regions considered in the jet counting analysis with 60 GeV jet p_T threshold, in the 1ℓ category (left) and the $2\ell^{sc}$ category (right). The pull is defined as the difference between the observed number of events and the total number of expected events determined by the fit divided by the total uncertainty. The total uncertainty is the sum in quadrature of the statistical error of the observed data and the uncertainty on the predicted background.

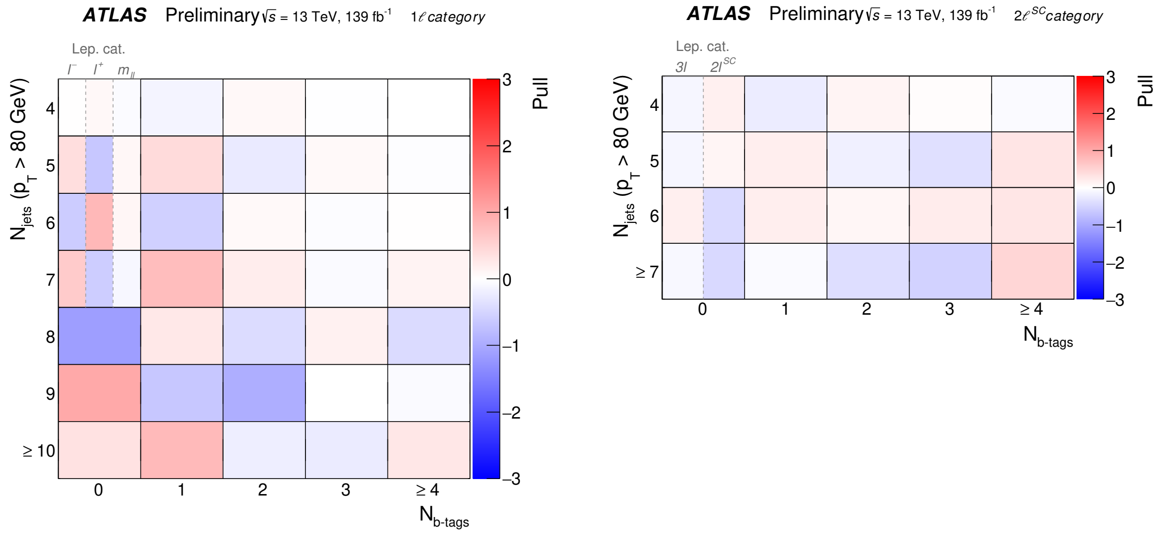

Figure 16: The observed pulls in all the regions considered in the jet counting analysis with 80 GeV jet p_{T} threshold, in the 1ℓ category (left) and the $2\ell^{\mathrm{sc}}$ category (right). The pull is defined as the difference between the observed number of events and the total number of expected events determined by the fit divided by the total uncertainty. The total uncertainty is the sum in quadrature of the statistical error of the observed data and the uncertainty on the predicted background.

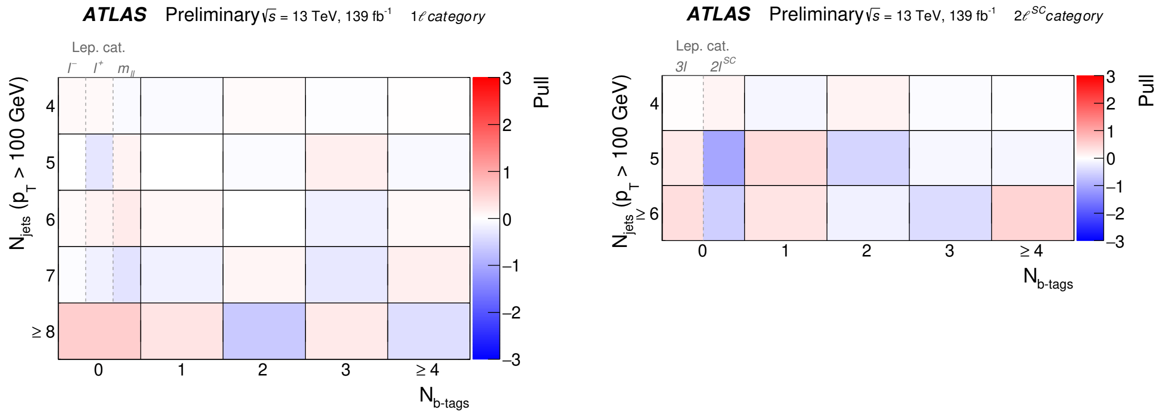

Figure 17: The observed pulls in all the regions considered in the jet counting analysis with 100 GeV jet p_{T} threshold, in the 1ℓ category (left) and the $2\ell^{\mathrm{sc}}$ category (right). The pull is defined as the difference between the observed number of events and the total number of expected events determined by the fit divided by the total uncertainty. The total uncertainty is the sum in quadrature of the statistical error of the observed data and the uncertainty on the predicted background.

References

[1] Y. Golfand and E. Likhtman, *Extension of the Algebra of Poincare Group Generators and Violation of P Invariance*, JETP Lett. **13** (1971) 323, [Pisma Zh. Eksp. Teor. Fiz. **13** (1971) 452] (cit. on p. 2).

[2] D. Volkov and V. Akulov, *Is the neutrino a goldstone particle?*, Phys. Lett. B **46** (1973) 109 (cit. on p. 2).

[3] J. Wess and B. Zumino, *Supergauge transformations in four dimensions*, Nucl. Phys. B **70** (1974) 39 (cit. on p. 2).

[4] J. Wess and B. Zumino, *Supergauge invariant extension of quantum electrodynamics*, Nucl. Phys. B **78** (1974) 1 (cit. on p. 2).

[5] S. Ferrara and B. Zumino, *Supergauge invariant Yang-Mills theories*, Nucl. Phys. B **79** (1974) 413 (cit. on p. 2).

[6] A. Salam and J. Strathdee, *Super-symmetry and non-Abelian gauges*, Phys. Lett. B **51** (1974) 353 (cit. on p. 2).

[7] N. Sakai, *Naturalness in supersymmetric GUTS*, Z. Phys. C **11** (1981) 153 (cit. on p. 2).

[8] S. Dimopoulos, S. Raby and F. Wilczek, *Supersymmetry and the scale of unification*, Phys. Rev. D **24** (1981) 1681 (cit. on p. 2).

[9] L. E. Ibáñez and G. G. Ross, *Low-energy predictions in supersymmetric grand unified theories*, Phys. Lett. B **105** (1981) 439 (cit. on p. 2).

[10] S. Dimopoulos and H. Georgi, *Softly broken supersymmetry and SU(5)*, Nucl. Phys. B **193** (1981) 150 (cit. on p. 2).

[11] G. R. Farrar and P. Fayet, *Phenomenology of the production, decay, and detection of new hadronic states associated with supersymmetry*, Phys. Lett. B **76** (1978) 575 (cit. on p. 2).

[12] H. Goldberg, *Constraint on the Photino Mass from Cosmology*, Phys. Rev. Lett. **50** (1983) 1419 (cit. on p. 2), Erratum: Phys. Rev. Lett. **103** (2009) 099905.

[13] J. Ellis, J. Hagelin, D. V. Nanopoulos, K. A. Olive and M. Srednicki, *Supersymmetric relics from the big bang*, Nucl. Phys. B **238** (1984) 453 (cit. on p. 2).

[14] J. A. Evans, Y. Kats, D. Shih and M. J. Strassler, *Toward Full LHC Coverage of Natural Supersymmetry*, JHEP **07** (2014) 101, arXiv: `1310.5758 [hep-ph]` (cit. on p. 2).

[15] B. Batell, T. Lin and L.-T. Wang, *Flavored Dark Matter and R-Parity Violation*, JHEP **01** (2014) 075, arXiv: `1309.4462 [hep-ph]` (cit. on p. 2).

[16] G. D'Ambrosio, G. F. Giudice, G. Isidori and A. Strumia, *Minimal Flavour Violation: an effective field theory approach*, Nucl. Phys. B **645** (2002) 155, arXiv: `hep-ph/0207036` (cit. on pp. 2, 3).

[17] C. Cs*á*ki, Y. Grossman and B. Heidenreich, *MFV SUSY: A Natural Theory for R-Parity Violation*, Phys. Rev. D **85** (2012) 095009, arXiv: `1111.1239 [hep-ph]` (cit. on pp. 2, 3).

[18] D. E. Lopez-Fogliani and C. Munoz, *Proposal for a Supersymmetric Standard Model*, Phys. Rev. Lett. **97** (2006) 041801, arXiv: `hep-ph/0508297` (cit. on p. 2).

[19] J. Alwall, M.-P. Le, M. Lisanti and J. G. Wacker, *Searching for directly decaying gluinos at the Tevatron*, Phys. Lett. B **666** (2008) 34, arXiv: `0803.0019 [hep-ph]` (cit. on p. 2).

[20] J. Alwall, P. Schuster and N. Toro, *Simplified models for a first characterization of new physics at the LHC*, Phys. Rev. D **79** (2009) 075020, arXiv: `0810.3921 [hep-ph]` (cit. on p. 2).

[21] D. Alves et al., *Simplified models for LHC new physics searches*, J. Phys. G **39** (2012) 105005, arXiv: `1105.2838 [hep-ph]` (cit. on p. 2).

[22] ATLAS Collaboration, *Search for new phenomena in a lepton plus high jet multiplicity final state with the ATLAS experiment using* $\sqrt{s} = 13$ *TeV proton-proton collision data*, JHEP **09** (2017) 088, arXiv: `1704.08493 [hep-ex]` (cit. on pp. 2, 23).

[23] ATLAS Collaboration, *Search for phenomena beyond the Standard Model in events with large b-jet multiplicity using the ATLAS detector at the LHC*, Eur. Phys. J. C **81** (2021) 11, arXiv: `2010.01015 [hep-ex]` (cit. on pp. 2, 27).

[24] ATLAS Collaboration, *Search for squarks and gluinos in final states with same-sign leptons and jets using 139* fb^{-1} *of data collected with the ATLAS detector*, JHEP **06** (2020) 046, arXiv: `1909.08457 [hep-ex]` (cit. on p. 2).

[25] ATLAS Collaboration, *Search for supersymmetry in events with four or more leptons in* $\sqrt{s} = 13$ *TeV pp collisions with ATLAS*, Phys. Rev. D **98** (2018) 032009, arXiv: `1804.03602 [hep-ex]` (cit. on p. 2).

[26] ATLAS Collaboration, *Search for R-parity-violating supersymmetric particles in multi-jet final states produced in p-p collisions at* $\sqrt{s} = 13$ *TeV using the ATLAS detector at the LHC*, Phys. Lett. B **785** (2018) 136, arXiv: `1804.03568 [hep-ex]` (cit. on p. 2).

[27] ATLAS Collaboration, *A search for pair-produced resonances in four-jet final states at* $\sqrt{s} = 13$ *TeV with the ATLAS detector*, Eur. Phys. J. C **78** (2018) 250, arXiv: `1710.07171 [hep-ex]` (cit. on pp. 2, 27).

[28] ATLAS Collaboration, *Search for B-L R -parity-violating top squarks in* $\sqrt{s}$ *=13 TeV pp collisions with the ATLAS experiment*, Phys. Rev. D **97** (2018) 032003, arXiv: `1710.05544 [hep-ex]` (cit. on p. 2).

[29] ATLAS Collaboration, *Search for supersymmetry in final states with two same-sign or three leptons and jets using 36* fb^{-1} *of* $\sqrt{s} = 13$ *TeV pp collision data with the ATLAS detector*, JHEP **09** (2017) 084, [Erratum: JHEP 08, 121 (2019)], arXiv: `1706.03731 [hep-ex]` (cit. on p. 2).

[30] CMS Collaboration, *Search for R-parity violating supersymmetry in pp collisions at* $\sqrt{s} = 13$ *TeV using b jets in a final state with a single lepton, many jets, and high sum of large-radius jet masses*, Phys. Lett. B **783** (2018) 114, arXiv: `1712.08920 [hep-ex]` (cit. on p. 2).

[31] CMS Collaboration, *Searches for R-parity-violating supersymmetry in ppcollisions at* $\sqrt{(s)} = 8$ *TeV in final states with 0-4 leptons*, Phys. Rev. D **94** (2016) 112009, arXiv: `1606.08076 [hep-ex]` (cit. on p. 2).

[32] CMS Collaboration, *Search for Top Squarks in R-Parity-Violating Supersymmetry using Three or More Leptons and B-Tagged Jets*, Phys. Rev. Lett. **111** (2013) 221801, arXiv: `1306.6643 [hep-ex]` (cit. on p. 2).

[33] ATLAS Collaboration, *Evidence for* $t\bar{t}t\bar{t}$ *production in the multilepton final state in proton-proton collisions at* $\sqrt{s} = 13$ *TeV with the ATLAS detector*, Eur. Phys. J. C **80** (2020) 1085, arXiv: `2007.14858 [hep-ex]` (cit. on pp. 2, 8, 19, 25).

[34] CMS Collaboration, *Search for standard model production of four top quarks in proton-proton collisions at* $\sqrt{s} = 13$ *TeV*, (2017), arXiv: `1702.06164 [hep-ex]` (cit. on p. 2).

[35] ATLAS Collaboration, *Search for long-lived, massive particles in events with displaced vertices and missing transverse momentum in* $\sqrt{s} = 13$ *TeV pp collisions with the ATLAS detector*, Phys. Rev. D **97** (2018) 052012, arXiv: `1710.04901 [hep-ex]` (cit. on p. 3).

[36] ATLAS Collaboration, *Search for long-lived, massive particles in events with a displaced vertex and a muon with large impact parameter in pp collisions at $\sqrt{s} = 13$ TeV with the ATLAS detector*, Phys. Rev. D **102** (2020) 032006, arXiv: `2003.11956 [hep-ex]` (cit. on p. 3).

[37] W. Beenakker et al., *The Production of Charginos/Neutralinos and Sleptons at Hadron Colliders*, Phys. Rev. Lett. **83** (1999) 3780, arXiv: `hep-ph/9906298` (cit. on pp. 3, 6), Erratum: Phys. Rev. Lett. **100** (2008) 029901.

[38] G. Bozzi, B. Fuks and M. Klasen, *Threshold Resummation for Slepton-Pair Production at Hadron Colliders*, Nucl. Phys. B **777** (2007) 157, arXiv: `hep-ph/0701202 [hep-ph]` (cit. on pp. 3, 6).

[39] B. Fuks, M. Klasen, D. R. Lamprea and M. Rothering, *Precision predictions for electroweak superpartner production at hadron colliders with RESUMMINO*, Eur. Phys. J. C **73** (2013) 2480, arXiv: `1304.0790 [hep-ph]` (cit. on pp. 3, 6).

[40] B. Fuks, M. Klasen, D. R. Lamprea and M. Rothering, *Revisiting slepton pair production at the Large Hadron Collider*, JHEP **01** (2014) 168, arXiv: `1310.2621 [hep-ph]` (cit. on pp. 3, 6).

[41] J. Fiaschi and M. Klasen, *Slepton pair production at the LHC in NLO+NLL with resummation-improved parton densities*, JHEP **03** (2018) 094, arXiv: `1801.10357 [hep-ph]` (cit. on pp. 3, 6).

[42] ATLAS Collaboration, *The ATLAS Experiment at the CERN Large Hadron Collider*, JINST **3** (2008) S08003 (cit. on p. 5).

[43] ATLAS Collaboration, *ATLAS Insertable B-Layer Technical Design Report*, ATLAS-TDR-19, 2010, URL: `https://cds.cern.ch/record/1291633`, *ATLAS Insertable B-Layer Technical Design Report Addendum*, ATLAS-TDR-19-ADD-1, 2012, URL: `https://cds.cern.ch/record/1451888` (cit. on p. 5).

[44] B. Abbott et al., *Production and integration of the ATLAS Insertable B-Layer*, JINST **13** (2018) T05008, arXiv: `1803.00844 [physics.ins-det]` (cit. on p. 5).

[45] ATLAS Collaboration, *The performance of the jet trigger for the ATLAS detector during 2011 data taking*, Eur. Phys. J. C **76** (2016) 526, arXiv: `1606.07759 [hep-ex]` (cit. on p. 5).

[46] S. Agostinelli et al., *GEANT4: A Simulation toolkit*, Nucl. Instrum. Meth. **A506** (2003) 250 (cit. on p. 5).

[47] ATLAS Collaboration, *The ATLAS Simulation Infrastructure*, Eur.Phys.J. **C70** (2010) 823, arXiv: `1005.4568 [physics.ins-det]` (cit. on p. 5).

[48] T. Sjöstrand et al., *An introduction to PYTHIA 8.2*, Comput. Phys. Commun. **191** (2015) 159, arXiv: `1410.3012 [hep-ph]` (cit. on pp. 5, 6).

[49] R. D. Ball et al., *Parton distributions with LHC data*, Nucl. Phys. B **867** (2013) 244, arXiv: `1207.1303 [hep-ph]` (cit. on pp. 5, 6).

[50] ATLAS Collaboration, *The Pythia 8 A3 tune description of ATLAS minimum bias and inelastic measurements incorporating the Donnachie–Landshoff diffractive model*, ATL-PHYS-PUB-2016-017, 2016, URL: `https://cds.cern.ch/record/2206965` (cit. on p. 5).

[51] D. J. Lange, *The EvtGen particle decay simulation package*, Nucl. Instrum. Meth. A **462** (2001) 152 (cit. on p. 5).

[52] J. Alwall et al., *The automated computation of tree-level and next-to-leading order differential cross sections, and their matching to parton shower simulations*, JHEP **07** (2014) 079, arXiv: `1405.0301 [hep-ph]` (cit. on p. 6).

[53] ATLAS Collaboration, *The ATLAS Simulation Infrastructure*, Eur. Phys. J. C **70** (2010) 823, arXiv: `1005.4568 [physics.ins-det]` (cit. on p. 6).

[54] ATLAS Collaboration, *The simulation principle and performance of the ATLAS fast calorimeter simulation FastCaloSim*, ATL-PHYS-PUB-2010-013, 2010, URL: `https://cds.cern.ch/record/1300517` (cit. on p. 6).

[55] W. Beenakker, C. Borschensky, M. Krämer, A. Kulesza and E. Laenen, *NNLL-fast: predictions for coloured supersymmetric particle production at the LHC with threshold and Coulomb resummation*, JHEP **12** (2016) 133, arXiv: `1607.07741 [hep-ph]` (cit. on p. 6).

[56] W. Beenakker et al., *NNLL resummation for squark and gluino production at the LHC*, JHEP **12** (2014) 023, arXiv: `1404.3134 [hep-ph]` (cit. on p. 6).

[57] W. Beenakker et al., *Towards NNLL resummation: hard matching coefficients for squark and gluino hadroproduction*, JHEP **10** (2013) 120, arXiv: `1304.6354 [hep-ph]` (cit. on p. 6).

[58] W. Beenakker et al., *NNLL resummation for squark-antisquark pair production at the LHC*, JHEP **01** (2012) 076, arXiv: `1110.2446 [hep-ph]` (cit. on p. 6).

[59] W. Beenakker et al., *Soft-gluon resummation for squark and gluino hadroproduction*, JHEP **12** (2009) 041, arXiv: `0909.4418 [hep-ph]` (cit. on p. 6).

[60] A. Kulesza and L. Motyka, *Soft gluon resummation for the production of gluino-gluino and squark-antisquark pairs at the LHC*, Phys. Rev. D **80** (2009) 095004, arXiv: `0905.4749 [hep-ph]` (cit. on p. 6).

[61] A. Kulesza and L. Motyka, *Threshold resummation for squark-antisquark and gluino-pair production at the LHC*, Phys. Rev. Lett. **102** (2009) 111802, arXiv: `0807.2405 [hep-ph]` (cit. on p. 6).

[62] W. Beenakker, R. Höpker, M. Spira and P. Zerwas, *Squark and gluino production at hadron colliders*, Nucl. Phys. B **492** (1997) 51, arXiv: `hep-ph/9610490` (cit. on p. 6).

[63] W. Beenakker, M. Krämer, T. Plehn, M. Spira and P. Zerwas, *Stop production at hadron colliders*, Nucl. Phys. B **515** (1998) 3, arXiv: `hep-ph/9710451` (cit. on p. 6).

[64] W. Beenakker et al., *Supersymmetric top and bottom squark production at hadron colliders*, JHEP **08** (2010) 098, arXiv: `1006.4771 [hep-ph]` (cit. on p. 6).

[65] W. Beenakker et al., *NNLL resummation for stop pair-production at the LHC*, JHEP **05** (2016) 153, arXiv: `1601.02954 [hep-ph]` (cit. on p. 6).

[66] E. Bothmann et al., *Event generation with Sherpa 2.2*, SciPost Phys. **7** (2019) 034, arXiv: `1905.09127 [hep-ph]` (cit. on p. 6).

[67] C. Anastasiou, L. J. Dixon, K. Melnikov and F. Petriello, *High precision QCD at hadron colliders: Electroweak gauge boson rapidity distributions at next-to-next-to leading order*, Phys. Rev. D **69** (2004) 094008, arXiv: `hep-ph/0312266` (cit. on p. 6).

[68] R. D. Ball et al., *Parton distributions for the LHC run II*, JHEP **04** (2015) 040, arXiv: `1410.8849 [hep-ph]` (cit. on p. 6).

[69] T. Sjöstrand, S. Mrenna and P. Skands, *A brief introduction to PYTHIA 8.1*, Comput. Phys. Commun. **178** (2008) 852, arXiv: `0710.3820 [hep-ph]` (cit. on p. 6).

[70] ATLAS Collaboration, *ATLAS Pythia 8 tunes to 7 TeV data*, ATL-PHYS-PUB-2014-021, 2014, URL: `https://cds.cern.ch/record/1966419` (cit. on p. 6).

[71] S. Frixione, P. Nason and G. Ridolfi, *A Positive-Weight Next-to-Leading-Order Monte Carlo for Heavy Flavour Hadroproduction*, JHEP **09** (2007) 126, arXiv: `0707.3088 [hep-ph]` (cit. on p. 6).

[72] P. Nason, *A New Method for Combining NLO QCD with Shower Monte Carlo Algorithms*, JHEP **11** (2004) 040, arXiv: `hep-ph/0409146` (cit. on p. 6).

[73] S. Frixione, P. Nason and C. Oleari, *Matching NLO QCD computations with Parton Shower simulations: the POWHEG method*, JHEP **11** (2007) 070, arXiv: `0709.2092 [hep-ph]` (cit. on p. 6).

[74] S. Alioli, P. Nason, C. Oleari and E. Re, *A general framework for implementing NLO calculations in shower Monte Carlo programs: the POWHEG BOX*, JHEP **06** (2010) 043, arXiv: `1002.2581 [hep-ph]` (cit. on p. 6).

[75] M. Beneke, P. Falgari, S. Klein and C. Schwinn, *Hadronic top-quark pair production with NNLL threshold resummation*, Nucl. Phys. B **855** (2012) 695, arXiv: `1109.1536 [hep-ph]` (cit. on p. 6).

[76] M. Cacciari, M. Czakon, M. Mangano, A. Mitov and P. Nason, *Top-pair production at hadron colliders with next-to-next-to-leading logarithmic soft-gluon resummation*, Phys. Lett. B **710** (2012) 612, arXiv: `1111.5869 [hep-ph]` (cit. on p. 6).

[77] P. Bärnreuther, M. Czakon and A. Mitov, *Percent-Level-Precision Physics at the Tevatron: Next-to-Next-to-Leading Order QCD Corrections to* $q\bar{q} \to t\bar{t} + X$, Phys. Rev. Lett. **109** (2012) 132001, arXiv: `1204.5201 [hep-ph]` (cit. on p. 6).

[78] M. Czakon and A. Mitov, *NNLO corrections to top-pair production at hadron colliders: the all-fermionic scattering channels*, JHEP **12** (2012) 054, arXiv: `1207.0236 [hep-ph]` (cit. on p. 6).

[79] M. Czakon and A. Mitov, *NNLO corrections to top pair production at hadron colliders: the quark-gluon reaction*, JHEP **01** (2013) 080, arXiv: `1210.6832 [hep-ph]` (cit. on p. 6).

[80] M. Czakon, P. Fiedler and A. Mitov, *Total Top-Quark Pair-Production Cross Section at Hadron Colliders Through* $O(\alpha_S^4)$, Phys. Rev. Lett. **110** (2013) 252004, arXiv: `1303.6254 [hep-ph]` (cit. on p. 6).

[81] M. Czakon and A. Mitov, *Top++: A program for the calculation of the top-pair cross-section at hadron colliders*, Comput. Phys. Commun. **185** (2014) 2930, arXiv: `1112.5675 [hep-ph]` (cit. on p. 6).

[82] M. Bähr et al., *Herwig++ physics and manual*, Eur. Phys. J. C **58** (2008) 639, arXiv: `0803.0883 [hep-ph]` (cit. on p. 6).

[83] J. Bellm et al., *Herwig 7.0/Herwig++ 3.0 release note*, Eur. Phys. J. C **76** (2016) 196, arXiv: `1512.01178 [hep-ph]` (cit. on p. 6).

[84] L. Harland-Lang, A. Martin, P. Motylinski and R. Thorne, *Parton distributions in the LHC era: MMHT 2014 PDFs*, Eur. Phys. J. C **75** (2015) 204, arXiv: `1412.3989 [hep-ph]` (cit. on p. 6).

[85] S. Alioli, P. Nason, C. Oleari and E. Re, *NLO single-top production matched with shower in POWHEG: s- and t-channel contributions*, JHEP **09** (2009) 111, arXiv: `0907.4076 [hep-ph]` (cit. on p. 6), Erratum: JHEP **02** (2010) 011.

[86] E. Re, *Single-top Wt-channel production matched with parton showers using the POWHEG method*, Eur. Phys. J. C **71** (2011) 1547, arXiv: `1009.2450 [hep-ph]` (cit. on p. 6).

[87] R. Frederix, E. Re and P. Torrielli, *Single-top t-channel hadroproduction in the four-flavour scheme with POWHEG and aMC@NLO*, JHEP **09** (2012) 130, arXiv: `1207.5391 [hep-ph]` (cit. on p. 6).

[88] N. Kidonakis, *Next-to-next-to-leading-order collinear and soft gluon corrections for t-channel single top quark production*, Phys. Rev. D **83** (2011) 091503, arXiv: `1103.2792 [hep-ph]` (cit. on p. 6).

[89] N. Kidonakis, *Two-loop soft anomalous dimensions for single top quark associated production with a W^- or H^-*, Phys. Rev. D **82** (2010) 054018, arXiv: `1005.4451 [hep-ph]` (cit. on p. 6).

[90] N. Kidonakis, *Top Quark Production*, *Proceedings, Helmholtz International Summer School on Physics of Heavy Quarks and Hadrons (HQ 2013)* 139, arXiv: `1311.0283 [hep-ph]` (cit. on p. 6).

[91] R. Frederix, D. Pagani and M. Zaro, *Large NLO corrections in $t\bar{t}W^{\pm}$ and $t\bar{t}t\bar{t}$ hadroproduction from supposedly subleading EW contributions*, JHEP **02** (2018) 031, arXiv: `1711.02116 [hep-ph]` (cit. on pp. 6, 25).

[92] H. B. Hartanto, B. Jäger, L. Reina and D. Wackeroth, *Higgs boson production in association with top quarks in the POWHEG BOX*, Phys. Rev. D **91** (2015) 094003, arXiv: `1501.04498 [hep-ph]` (cit. on p. 6).

[93] T. Gleisberg and S. Höche, *Comix, a new matrix element generator*, JHEP **12** (2008) 039, arXiv: `0808.3674 [hep-ph]` (cit. on p. 6).

[94] F. Cascioli, P. Maierhöfer and S. Pozzorini, *Scattering Amplitudes with Open Loops*, Phys. Rev. Lett. **108** (2012) 111601, arXiv: `1111.5206 [hep-ph]` (cit. on p. 6).

[95] A. Denner, S. Dittmaier and L. Hofer, *Collier: A fortran-based complex one-loop library in extended regularizations*, Comput. Phys. Commun. **212** (2017) 220, arXiv: `1604.06792 [hep-ph]` (cit. on p. 6).

[96] S. Schumann and F. Krauss, *A parton shower algorithm based on Catani–Seymour dipole factorisation*, JHEP **03** (2008) 038, arXiv: `0709.1027 [hep-ph]` (cit. on p. 6).

[97] S. Höche, F. Krauss, M. Schönherr and F. Siegert, *A critical appraisal of NLO+PS matching methods*, JHEP **09** (2012) 049, arXiv: `1111.1220 [hep-ph]` (cit. on p. 6).

[98] S. Höche, F. Krauss, M. Schönherr and F. Siegert, *QCD matrix elements + parton showers. The NLO case*, JHEP **04** (2013) 027, arXiv: `1207.5030 [hep-ph]` (cit. on p. 6).

[99] S. Catani, F. Krauss, R. Kuhn and B. R. Webber, *QCD Matrix Elements + Parton Showers*, JHEP **11** (2001) 063, arXiv: `hep-ph/0109231` (cit. on p. 6).

[100] S. Höche, F. Krauss, S. Schumann and F. Siegert, *QCD matrix elements and truncated showers*, JHEP **05** (2009) 053, arXiv: `0903.1219 [hep-ph]` (cit. on p. 6).

[101] ATLAS Collaboration, *ATLAS data quality operations and performance for 2015–2018 data-taking*, JINST **15** (2020) P04003, arXiv: `1911.04632 [physics.ins-det]` (cit. on p. 7).

[102] ATLAS Collaboration, *Luminosity determination in pp collisions at $\sqrt{s}$ = 13 TeV using the ATLAS detector at the LHC*, ATLAS-CONF-2019-021, 2019, URL: `https://cds.cern.ch/record/2677054` (cit. on p. 7).

[103] G. Avoni et al., *The new LUCID-2 detector for luminosity measurement and monitoring in ATLAS*, JINST **13** (2018) P07017 (cit. on p. 7).

[104] ATLAS Collaboration, *Vertex Reconstruction Performance of the ATLAS Detector at $\sqrt{s}$ = 13 TeV*, ATL-PHYS-PUB-2015-026, 2015, URL: `https://cds.cern.ch/record/2037717` (cit. on p. 7).

[105] ATLAS Collaboration, *Reconstruction of primary vertices at the ATLAS experiment in Run 1 proton–proton collisions at the LHC*, Eur. Phys. J. C **77** (2017) 332, arXiv: `1611.10235 [hep-ex]` (cit. on p. 7).

[106] M. Cacciari, G. P. Salam and G. Soyez, *The anti-k_t jet clustering algorithm*, JHEP **04** (2008) 063, arXiv: `0802.1189 [hep-ph]` (cit. on p. 7).

[107] M. Cacciari, G. P. Salam and G. Soyez, *FastJet user manual*, Eur. Phys. J. C **72** (2012) 1896, arXiv: `1111.6097 [hep-ph]` (cit. on p. 7).

[108] ATLAS Collaboration, *Jet reconstruction and performance using particle flow with the ATLAS Detector*, Eur. Phys. J. C **77** (2017) 466, arXiv: `1703.10485 [hep-ex]` (cit. on pp. 7, 10).

[109] ATLAS Collaboration, *Jet energy scale and resolution measured in proton–proton collisions at $\sqrt{s} = 13$ TeV with the ATLAS detector*, (2020), arXiv: `2007.02645 [hep-ex]` (cit. on p. 7).

[110] ATLAS Collaboration, *Selection of jets produced in 13 TeV proton–proton collisions with the ATLAS detector*, ATLAS-CONF-2015-029, 2015, URL: `https://cds.cern.ch/record/2037702` (cit. on p. 7).

[111] ATLAS Collaboration, *Performance of pile-up mitigation techniques for jets in pp collisions at $\sqrt{s} = 8$ TeV using the ATLAS detector*, Eur. Phys. J. C **76** (2016) 581, arXiv: `1510.03823 [hep-ex]` (cit. on p. 7).

[112] ATLAS Collaboration, *ATLAS b-jet identification performance and efficiency measurement with $t\bar{t}$ events in pp collisions at $\sqrt{s} = 13$ TeV*, Eur. Phys. J. C **79** (2019) 970, arXiv: `1907.05120 [hep-ex]` (cit. on p. 7).

[113] ATLAS Collaboration, *Optimisation and performance studies of the ATLAS b-tagging algorithms for the 2017-18 LHC run*, ATL-PHYS-PUB-2017-013, 2017, URL: `https://cds.cern.ch/record/2273281` (cit. on p. 7).

[114] ATLAS Collaboration, *ATLAS b-jet identification performance and efficiency measurement with $t\bar{t}$ events in pp collisions at $\sqrt{s} = 13$ TeV*, Eur. Phys. J. C **79** (2019) 970, arXiv: `1907.05120 [hep-ex]` (cit. on p. 7).

[115] ATLAS Collaboration, *Electron and photon performance measurements with the ATLAS detector using the 2015–2017 LHC proton–proton collision data*, JINST **14** (2019) P12006, arXiv: `1908.00005 [hep-ex]` (cit. on pp. 7, 8).

[116] ATLAS Collaboration, *Muon reconstruction performance of the ATLAS detector in proton–proton collision data at $\sqrt{s} = 13$ TeV*, Eur. Phys. J. C **76** (2016) 292, arXiv: `1603.05598 [hep-ex]` (cit. on p. 8).

[117] ATLAS Collaboration, *Evidence for the associated production of the Higgs boson and a top quark pair with the ATLAS detector*, Phys. Rev. D **97** (2018) 072003, arXiv: `1712.08891 [hep-ex]` (cit. on p. 8).

[118] ATLAS Collaboration, *Performance of missing transverse momentum reconstruction with the ATLAS detector using proton–proton collisions at $\sqrt{s} = 13$ TeV*, Eur. Phys. J. C **78** (2018) 903, arXiv: `1802.08168 [hep-ex]` (cit. on p. 8).

[119] ATLAS Collaboration, *E_T^{miss} performance in the ATLAS detector using 2015–2016 LHC pp collisions*, ATLAS-CONF-2018-023, 2018, URL: `https://cds.cern.ch/record/2625233` (cit. on p. 8).

[120] ATLAS Collaboration, *Performance of the ATLAS muon triggers in Run 2*, JINST **15** (2020) P09015, arXiv: `2004.13447 [hep-ex]` (cit. on p. 9).

[121] ATLAS Collaboration, *Performance of electron and photon triggers in ATLAS during LHC Run 2*, Eur. Phys. J. C **80** (2020) 47, arXiv: `1909.00761 [hep-ex]` (cit. on p. 9).

[122] G. J. Székely, M. L. Rizzo and N. K. Bakirov, *Measuring and testing dependence by correlation of distances*, Ann. Statist. **35** (2007) 2769, URL: `https://doi.org/10.1214/009053607000000505` (cit. on p. 10).

[123] A. Paszke et al., *PyTorch: An Imperative Style, High-Performance Deep Learning Library*, *Advances in Neural Information Processing Systems 32*, Curran Associates, Inc., 2019 8024 (cit. on p. 11).

[124] D. P. Kingma and J. Ba, *Adam: A Method for Stochastic Optimization*, 2017, arXiv: `1412.6980 [cs.LG]` (cit. on p. 11).

[125] M. Sundararajan, A. Taly and Q. Yan, *Axiomatic Attribution for Deep Networks*, 2017, arXiv: `1703.01365 [cs.LG]` (cit. on p. 11).

[126] S. D. Ellis, R. Kleiss and W. J. Stirling, *W's, Z's and Jets*, Phys. Lett. B **154** (1985) 435 (cit. on p. 13).

[127] F. A. Berends, W. T. Giele, H. Kuijf, R. H. Kleiss and W. J. Stirling, *Multijet production in W, Z events at $p\bar{p}$ colliders*, Phys. Lett. B **224** (1989) 237 (cit. on p. 13).

[128] W. Giele and W. Stirling, *Top search at fermilab: Multijet signals and backgrounds*, Nucl. Phys. B **343** (1990) 14 (cit. on p. 13).

[129] E. Gerwick, T. Plehn, S. Schumann and P. Schichtel, *Scaling Patterns for QCD Jets*, JHEP **10** (2012) 162, arXiv: `1208.3676 [hep-ph]` (cit. on p. 13).

[130] ATLAS Collaboration, *Measurement of the production cross section of jets in association with a Z boson in pp collisions at $\sqrt{s} = 7$ TeV with the ATLAS detector*, JHEP **07** (2013) 032, arXiv: `1304.7098 [hep-ex]` (cit. on p. 13).

[131] ATLAS Collaboration, *Measurements of the production cross section of a Z boson in association with jets in pp collisions at $\sqrt{s} = 13$ TeV with the ATLAS detector*, (2017), arXiv: `1702.05725 [hep-ex]` (cit. on p. 13).

[132] CMS Collaboration, *Jet Production Rates in Association with W and Z Bosons in pp Collisions at $\sqrt{s} = 7$ TeV*, JHEP **01** (2012) 010, arXiv: `1110.3226 [hep-ex]` (cit. on p. 13).

[133] ATLAS Collaboration, *Search for supersymmetry at $\sqrt{s} = 13$ TeV in final states with jets and two same-sign leptons or three leptons with the ATLAS detector*, Eur. Phys. J. C **76** (2016) 259, arXiv: `1602.09058 [hep-ex]` (cit. on pp. 17, 19).

[134] ATLAS Collaboration, *Performance of missing transverse momentum reconstruction with the ATLAS detector in the first proton–proton collisions at $\sqrt{s} = 13$ TeV*, ATL-PHYS-PUB-2015-027, 2015, URL: `https://cds.cern.ch/record/2037904` (cit. on p. 17).

[135] ATLAS Collaboration, *Expected performance of missing transverse momentum reconstruction for the ATLAS detector at $\sqrt{s} = 13$ TeV*, ATL-PHYS-PUB-2015-023, 2015, URL: `https://cds.cern.ch/record/2037700` (cit. on p. 17).

[136] M. Botje et al., *The PDF4LHC Working Group Interim Recommendations*, (2011), arXiv: `1101.0538 [hep-ph]` (cit. on p. 18).

[137] G. Cowan, K. Cranmer, E. Gross and O. Vitells, *Asymptotic formulae for likelihood-based tests of new physics*, Eur. Phys. J. C **71** (2011) 1554, arXiv: `1007.1727 [physics.data-an]` (cit. on p. 20), Erratum: Eur. Phys. J. C **73** (2013) 2501.

[138] A. L. Read, *Presentation of search results: the CL_S technique*, J. Phys. G **28** (2002) 2693 (cit. on p. 20).

[139] DELPHI Collaboration, *Search for supersymmetric particles assuming R-parity non-conservation in e^+e^- collisions at $\sqrt{s}$ = 192 GeV to 208 GeV*, Eur. Phys. J. C **36** (2004) 1, [Erratum: Eur.Phys.J.C 37, 129–131 (2004)], arXiv: `hep-ex/0406009` (cit. on p. 29).

[140] A. Heister et al., *Search for supersymmetric particles with R parity violating decays in e^+e^- collisions at $\sqrt{s}$ up to 209-GeV*, Eur. Phys. J. C **31** (2003) 1, arXiv: `hep-ex/0210014` (cit. on p. 29).

[141] P. Achard et al., *Search for R parity violating decays of supersymmetric particles in e^+e^- collisions at LEP*, Phys. Lett. B **524** (2002) 65, arXiv: `hep-ex/0110057` (cit. on p. 29).